

8-2010

## Thoracic target volume delineation using various maximum-intensity projection computed tomography image sets for stereotactic body radiation therapy

David A. Zamora

Follow this and additional works at: [https://digitalcommons.library.tmc.edu/utgsbs\\_dissertations](https://digitalcommons.library.tmc.edu/utgsbs_dissertations)



Part of the [Other Medical Sciences Commons](#), and the [Other Physics Commons](#)

### Recommended Citation

Zamora, David A., "Thoracic target volume delineation using various maximum-intensity projection computed tomography image sets for stereotactic body radiation therapy" (2010). *The University of Texas MD Anderson Cancer Center UTHealth Graduate School of Biomedical Sciences Dissertations and Theses (Open Access)*. 62.

[https://digitalcommons.library.tmc.edu/utgsbs\\_dissertations/62](https://digitalcommons.library.tmc.edu/utgsbs_dissertations/62)

This Thesis (MS) is brought to you for free and open access by the The University of Texas MD Anderson Cancer Center UTHealth Graduate School of Biomedical Sciences at DigitalCommons@TMC. It has been accepted for inclusion in The University of Texas MD Anderson Cancer Center UTHealth Graduate School of Biomedical Sciences Dissertations and Theses (Open Access) by an authorized administrator of DigitalCommons@TMC. For more information, please contact [digitalcommons@library.tmc.edu](mailto:digitalcommons@library.tmc.edu).

THORACIC TARGET VOLUME DELINEATION USING VARIOUS  
MAXIMUM-INTENSITY PROJECTION COMPUTED TOMOGRAPHY  
IMAGE SETS FOR STEREOTACTIC BODY RADIATION THERAPY

by

David Anthony Zamora, BSME

APPROVED:

---

Tinsu Pan, Ph.D., Supervisory Professor

---

Peter Balter, Ph.D.

---

Valen Johnson, Ph.D.

---

Osama Mawlawi, Ph.D.

---

George Starkschall, Ph.D.

APPROVED:

---

George Stancel, Ph.D.

Dean, The University of Texas

Health Science Center at Houston

Graduate School of Biomedical Sciences at Houston

THORACIC TARGET VOLUME DELINEATION USING VARIOUS  
MAXIMUM-INTENSITY PROJECTION COMPUTED TOMOGRAPHY  
IMAGE SETS FOR STEREOTACTIC BODY RADIATION THERAPY

A

THESIS

Presented to the Faculty of  
The University of Texas  
Health Science Center at Houston  
and  
The University of Texas  
M.D. Anderson Cancer Center  
Graduate School of Biomedical Sciences  
in Partial Fulfillment

of the Requirements

for the Degree of

MASTER OF SCIENCE

by

David Anthony Zamora, BSME  
Houston, Texas

August 2010

## **Acknowledgments**

I would like to thank my advisor Dr. Tinsu Pan for his guidance throughout the course of this work. I started work with him knowing nothing of the real process of research, and am completing this as a better student and as a better physicist. Similarly, the insight that the distinguished members of my committee offered throughout the course of this project was essential to any success that I have had. Thank you for your time and for serving as an example to me.

I have been fortunate thus far to work in an institution filled with individuals that have not only educated me, but have encouraged me. To the numerous people with whom I have crossed paths, thank you for helping to make me a better person.

Finally, and most importantly, I must express my appreciation to my wife, Cortney. Her support, both emotionally and financially truly made this work possible. Thank you for the love and good humor that you so offer so freely to me. I could not have done it without you.



# THORACIC TARGET VOLUME DELINEATION USING VARIOUS MAXIMUM-INTENSITY PROJECTION COMPUTED TOMOGRAPHY IMAGE SETS FOR STEREOTACTIC BODY RADIATION THERAPY

David Anthony Zamora, BSME

Supervisory Professor: Tinsu Pan, Ph.D.

The motion of lung tumors during respiration makes the accurate delivery of radiation therapy to the thorax difficult because it increases the uncertainty of target position. The adoption of four-dimensional computed tomography (4D-CT) has allowed us to determine how a tumor moves with respiration for each individual patient. Using information acquired during a 4D-CT scan, we can define the target, visualize motion, and calculate dose during the planning phase of the radiotherapy process. One image data set that can be created from the 4D-CT acquisition is the maximum-intensity projection (MIP). The MIP can be used as a starting point to define the volume that encompasses the motion envelope of the moving gross target volume (GTV).

Because of the close relationship that exists between the MIP and the final target volume, we investigated four MIP data sets created with different methodologies (3 using various 4D-CT sorting implementations, and one using all available cine CT images) to compare target delineation. It has been observed that changing the 4D-CT sorting method will lead to the selection of a different collection of images; however, the clinical implications of changing the constituent images on the resultant MIP data set are not clear. There has not been a comprehensive study that compares target delineation based on different 4D-CT sorting methodologies in a patient population. We selected a collection of patients who had previously undergone thoracic 4D-CT scans at our institution, and who had lung tumors that moved at least 1 cm. We then generated the four MIP data sets and automatically contoured the target volumes.

In doing so, we identified cases in which the MIP generated from a 4D-CT sorting process under-represented the motion envelope of the target volume by more than 10% than when measured on the MIP generated from all of the cine CT images. The 4D-CT methods suffered from duplicate image selection and might not choose maximum extent images. Based on our results, we suggest utilization of a MIP generated from the full cine CT data set to ensure a representative inclusive tumor extent, and to avoid geometric miss.

## Table of Contents

1. PROJECT HYPOTHESIS AND SPECIFIC AIMS.....	1
2. INTRODUCTION .....	4
2.1 Four-Dimensional Computed Tomography (4D-CT) .....	6
2.1.1 Clinical Application of 4D-CT.....	7
2.1.2 Basic System Components for 4D-CT .....	8
2.1.3 Cine and Low-Pitch Helical 4D-CT Acquisitions.....	8
2.2 Cine CT Based 4D-CT with Varian Real-time Position Management System.....	11
2.2.1 Components of Varian RPM Data File .....	15
2.3 External Beam Radiation Therapy and 4D-CT .....	16
2.3.1 Maximum-Intensity Projection Images for Target Delineation .....	17
2.3.2 Current Clinical Protocol for Cine Based 4D-CT .....	19
2.3.3 4D-CT and Thoracic Treatment Planning.....	21
3. SPECIFIC AIM 1: PATIENT SELECTION AND IMAGE PROCESSING .....	24
3.1 Objectives.....	24
3.2 Materials and Methods.....	24
3.2.1 Patient Selection Criterion .....	28
3.2.2 Development of Maximum Intensity Projection Images – Sorting Software .....	28
3.2.2.1 Implementation of Phase-Binning [PB] .....	30
3.2.2.2 Implementation of Phase-corrected Phase-Binning [PC-PB] .....	30
3.2.2.3 Implementation of Amplitude-Binning [AB].....	32
3.2.2.4 4D-CT Sorting Mechanism Summary and Example.....	34
3.2.3 RPM File Timing Calculations .....	35
3.3 Results.....	36
4. SPECIFIC AIM 2: VOLUME MEASUREMENTS ON MIP DATA SETS.....	37
4.1 Objectives.....	37

4.2	Methods and Materials.....	37
4.2.1	Characterization of Tumor Size .....	38
4.2.2	Pinnacle Automatic Contouring.....	38
4.2.3	Pinnacle Volume Calculations .....	41
4.2.4	Simulated Margin Expansion of iGTV .....	42
4.3	Results.....	42
5.	SPECIFIC AIM 3: INVESTIGATION OF CAUSES OF IGTV DIFFERENCES .....	49
5.1	Objectives.....	49
5.2	Methods and Materials.....	49
5.2.1	Composite Overlay of Respiratory Trace and Selected 4D-CT Images.....	49
5.2.1.1	Temporal Alignment of RPM Data and Image Mid-scan Times .....	50
5.2.1.2	Compiling Respiratory and Image Data.....	55
5.3	Results.....	56
5.3.1	Duplicate Image Selection .....	56
5.3.2	Error in Selection of Maximum Extent Image .....	60
6.	DISCUSSION .....	62
6.1	Clinical Recommendations .....	62
6.2	Future Work .....	65
7.	CONCLUSIONS .....	67
8.	BIBLIOGRAPHY .....	68
9.	VITA.....	73

## List of Figures

Figure 1: Schematic of axial and cine image acquisition.....	10
Figure 2: Calculation of numerical phase with respiratory surrogate. ....	13
Figure 3: Hardware for cine CT based 4D-CT with Varian RPM. ....	14
Figure 4: 4D-CT phase-binning selection process.....	15
Figure 5: Conventional and stereotactic dose delivery schedules.....	17
Figure 6: Clinical example of diaphragm over-writing tumor in MIP.....	18
Figure 7: Radiation therapy general workflow. ....	21
Figure 8: Definition of margin expansions to gross target volume (GTV).....	23
Figure 9: MIP images generated in this study.....	27
Figure 10: Project workflow for performing data processing.....	29
Figure 11: User interface for 4D-CT sorting and image processing software. ....	30
Figure 12: User interface of phase-correct software.....	32
Figure 13: Example of amplitude-binning applied to a single bed position. ....	34
Figure 14: 4D-CT summary selection process for PB, PC-PB, and AB.....	35
Figure 15: Automatic contouring tools within treatment planning system.....	40
Figure 16: Volume calculations using Pinnacle treatment planning system.....	41
Figure 17: Margin expansion applied to iGTV.....	42
Figure 18: Histogram of target volume results. ....	48
Figure 19: Relationship between mid-scan time and image temporal window. ....	51
Figure 20: Graphical representation of RPM and image time alignment. ....	52
Figure 21: Schematic exhibiting beam on/off calculations from cine images. ....	53
Figure 22: Example of respiratory waveform and image composite overlay. ....	56
Figure 23: Cause of duplicate image selection in PC-PB and AB.....	57
Figure 24: Distribution of duplicate image selection by adjacent bin pair. ....	58
Figure 25: Regions of high phase- and amplitude-rate on respiratory waveform.....	59
Figure 26: Clinical example of error in selection of maximum extent image.....	61
Figure 27: Temporal window of CT image. ....	63
Figure 28: MIP images for PB and PC-PB clinical example.....	64

## **List of Tables**

Table 1: Contents of respiratory monitoring RPM data file. ....	16
Table 2: Summary of measured iGTV values.....	44
Table 3: Paired t-test results comparing iGTV measurements.....	45
Table 4: Paired t-test results comparing PTV measurements. ....	46
Table 5: Summary of measured PTV values. ....	47
Table 6: Sample beam on/off calculations from RPM and cine CT images. ....	53
Table 7: Sample calculation of image mid-scan time correction factors. ....	55

## Abbreviations

3D	Three-dimensional
4D-CT	Four-dimensional Computed Tomography
AB	Amplitude-Binned
AP	Anterior-posterior
AW	Advantage Workstation
BW	Beam Width
CT	Computed Tomography
CTV	Clinical Target Volume
DFOV	Display Field of View
DICOM	Digital Imaging and Communications in Medicine
EBRT	External Beam Radiation Therapy
EE	End Expiration
EI	End Inspiration
FB	Free Breathing
GE	General Electric
Gy	Gray – unit of absorbed dose
Gy/fx	Dose (Gy) delivered per fraction (fx)
HU	Hounsfield Unit
iGTV	Internal Gross Target Volume
LR	Left-Right
mip	Minimum-Intensity Projection
MIP	Maximum-Intensity Projection
PB	Phase-Binned
PC	Phase-correct(-ed / -ing)
PC-PB	Phase-corrected Phase-Binned
PTV	Planning Target Volume
RAC	Respiratory Averaged Computed Tomography
ROI	Region of Interest
RPM	Real-time Position Management
RTOG	Radiation Therapy Oncology Group
SBRT	Stereotactic Body Radiation Therapy
SI	Superior-Inferior
TPS	Treatment Planning System

## 1. PROJECT HYPOTHESIS AND SPECIFIC AIMS

The motion of lung tumors during respiration is problematic when planning for radiation therapy treatment to the thorax. To address the issue of target motion, a respiratory surrogate has been introduced to track the breathing process. The information from the respiratory surrogate is used to distribute acquired CT images into image bins that represent different phases of the breathing cycle. From these binned images, one can gain an understanding of how the tumor is moving as the patient breathes. Different methods of image selection in the four-dimensional computed tomography (4D-CT) sorting process have been proposed, including phase- and amplitude-binning. Each 4D-CT binning method leads to the selection of a different set of images from the full cine CT data set.

From the 4D-CT images, a maximum-intensity-projection (MIP) image set can be created, which displays the maximum CT number of all the pixels at the same spatial location over the respiratory cycle. At our institution, the MIP data set is used as a starting point to define the volume that encompasses the motion envelope of the moving tumor, or the internal gross tumor volume (iGTV). Our goal is to quantify and to understand how varying the constituent images of the MIP data set leads to different initial iGTVs. We hope to determine the variations of the MIP images from 4D-CT images and from the entire cine CT image in terms of the largest tumor motion extent

**We hypothesize that MIPs created from cine data sets using various image selection methods will give different apparent iGTV volumes, with the range of differences in volume being greater than 10%. Examination of the selection process may help us understand the appropriate dataset to be used in estimating radiotherapy target volumes of mobile tumors.**

To test our hypothesis, we propose the following specific aims:

- 1) Identify a collection of lung cancer patients that exhibit respiratory-induced tumor motion of at least 1 cm. For each patient, we will obtain a full cine CT MIP, as well as 4D-CT MIPs generated from three different sorting methods: 1) phase-binned (PB) using retrospective

calculations 2) phase-corrected phase-binned (PC-PB) based on motion extrema 3) amplitude-binned (AB).

*Methodology* – From the existing 4D-CT patient archive, identify patients with lung tumor motion of at least 1 cm by measuring the total excursion distance on a standard three-plane view. Attain and phase-correct the corresponding respiratory files. Use in-house sorting software to perform phase and amplitude binning and then to create MIP image data sets. Characterize static tumor dimensions using a stationary phase image set near end-expiration.

2) Determine which set of MIP images most completely captures the lung tumor motion extent.

*Methodology* – Export the four MIP data sets to a radiation therapy treatment planning system. Using available automatic contouring tools, we delineate the tumor iGTV to find the total tumor motion envelope captured by each method. Apply clinical margins suggested in the literature (1) to observe differences in final planning target volume (PTV). Statistically analyze the results to highlight any differences in the contoured data sets, and identify any volume under-estimations when compared to cine MIP.

3) Compare the distribution of 4D-CT images selected and determine the underlying cause of volume differences.

*Methodology* – Design a method of displaying a composite overlay of the respiratory waveform and the time-corrected 4D-CT images to understand the root cause of observed volume differences. Develop a program to pull pertinent information from selected images to track all stages of the 4D-CT process.

By performing the aforementioned specific aims, we will test our hypothesis while gaining insight on how to improve current clinical practice. This study is significant because of the close relationship that exists between images generated in a therapy simulation and the final treatment volume. Different methods of 4D-CT image sorting have been proposed and implemented, and phantom studies that have been performed indicate that a move toward amplitude-binning would be beneficial in capturing tumor motion extent (2, 3). However, there is currently a lack of proof that



any sorting method is superior when defining iGTV when applied to clinical cases. Similarly, a lack of understanding exists as to why differences in volume may appear. This work aims to address both the issue of volume difference and the identification of the root cause of measured volume differences.

## 2. INTRODUCTION

The motion of lung tumors during respiration has to be considered when planning radiation therapy treatment to the thorax (4-7). Motion decreases the reproducibility of target position (6, 8) and can ultimately lead to larger margins during radiation therapy treatment planning (9-12). A readily available predictor (such as tumor size or location) of tumor motion does not currently exist (13); instead of relying upon population-based data and generalized target volume expansions (12), it is desirable to individually assess tumor motion for all patients (13).

The development of four-dimensional computed tomography (4D-CT) has enabled us to explicitly address the issue of target volume motion for individual patients (7). 4D-CT relies on a respiratory surrogate to track one of several physiological respiratory processes, such as exterior chest wall motion or air flow during breathing (14). While the respiratory motion is tracked, CT data are acquired over the volume of interest. By combining information from the respiratory surrogate and the CT data, a collection of images can be created that represents different stages of the breathing process. In this collection of images, we can visualize how a particular lung tumor moves during respiration.

Current 4D-CT scanning techniques fall in to one of two general categories: (1) cine CT acquisition with *image* sorting (15); and (2) low-pitch helical acquisition with *sinogram* binning (16). In image sorting with cine CT, images are acquired with the table stationary for a time interval over at least a respiratory cycle. The table is then indexed to the next position and additional images are acquired. Acquisition is followed by indexing until the desired volume has been scanned. The cine CT images and respiratory waveform are associated, and a subset of images that correspond to different snapshots of the tumor motion during respiration is selected (15). In sinogram binning, data is acquired with low-pitch helical acquisition, and the selection of target phases or amplitudes is made prior to image reconstruction in the sinogram projection data. Images are reconstructed around the identified target phases from the stream of sinogram data (16, 17). In both scanning techniques, the selected or reconstructed images are used to depict one respiratory cycle of the tumor motion. In

practice, CT data (both cine and low-pitch helical) are collected for longer than one respiratory cycle to capture sufficient projection data (17) and to account for potential variation in respiration during the CT data acquisition.

Regarding image sorting with cine CT, two primary methods of image selection, or binning, have been previously implemented: phase binning (PB) and amplitude binning (AB). In the PB method, images are selected to correspond to different phases of the respiratory waveform as calculated within the respiratory monitoring file (18, 19). The more recent AB implementation is based on measured amplitude and images are selected based on temporally associated amplitude and direction of respiration (i.e., inspiration or expiration) (2, 20). The selected 4D-CT images are a subset of the cine CT image set. Both of these sorting processes result in the generation of multiple phases of 3D image sets, called the 4D-CT image set.

From the 4D-CT image set, a maximum-intensity-projection (MIP) image, consisting of a pixel-by-pixel maximum CT number, can be generated (15). An identical process can be used to create a MIP from the entire unsorted cine CT image set. The MIP image set should ideally highlight the volume encompassing the location of the moving tumor at any point during respiration. Prior studies have investigated the level of utility and accuracy of target volume delineation with MIP images (21, 22). Rietzel *et al* showed that the contours generated on 4D-CT phase images were very similar to those on 4D-CT MIP (23). At our institution, the MIP from the 4D-CT data subset ( $\text{MIP}_{4\text{D-CT}}$ ) is used as a starting point to define the volume that encompasses the motion envelope of the moving gross target volume (GTV). This motion envelope has been named the internal gross target volume (iGTV).

It has been observed that changing the 4D-CT binning method leads to the selection of a different collection of images (2); however, the clinical implications of changing the constituent images on the resultant MIP data set are not clear. Prior studies have advocated the advantages of AB over PB in 4D-CT image selection either from a phantom study (2) or limited patient studies (3). In the phantom study, the correlation between the external surrogate and the internal tumor motion was ideal without

phase lag.. The patient studies were limited in the number of patients and the magnitude of motion. To our knowledge there has not been a comprehensive study to compare target volume delineation based on different 4D-CT sorting methodologies in a patient population. In a phantom study with irregular target motion, Park *et al* noted that the MIP can underestimate target motion (22). We believe that clinical situations exist in which the currently utilized 4D-CT based MIP will under-represent the visible motion envelope of the moving lung tumor. The purpose of this study was to quantify the differences in automatically contoured target volumes for usage in the delivery of stereotactic body radiation therapy (SBRT) based on maximum intensity projections (MIP) data sets generated from one of four methods: (1) phase-binned (PB) based on retrospective phase calculations; (2) phase-corrected phase-binned (PC-PB) based on a modified calculation of phase using motion extrema; (3) amplitude-binned (AB); and (4) cine CT built from all available images. By doing so, we can determine the degree to which the 4D-CT selection process under-represents the extent of tumor motion in patient cases.

The following subsections offer background information related to 4D-CT as it is utilized in the delivery of radiation therapy. Information is organized from general to specific, with a particular focus on applications, process workflows, and methods of acquisition. Further detail is also provided with regard to how images created with 4D-CT are utilized in the planning phase of the delivery of stereotactic body radiation therapy (SBRT).

## **2.1 Four-Dimensional Computed Tomography (4D-CT)**

Four-dimensional computed tomography (4D-CT) is a method of visualizing internal anatomical movement that is caused primarily by respiration. By performing a 4D-CT scan for patients that are to be treated with external beam radiation therapy (EBRT) to the thorax, we can individually assess target volume motion and can better adapt the delivery of radiation treatment to the individual patient. The following subsections discuss the clinical application of 4D-CT, and the basic components and the acquisition types used in 4D-CT.

### **2.1.1      *Clinical Application of 4D-CT***

The movement of a target volume due to respiration is an important consideration in radiation therapy to the thorax (24). In 2001, Stevens *et al* reported that easily determinable parameters such as pulmonary function, tumor size, and tumor location did not correlate strongly to the degree of lung tumor motion with respiration (13). The development of 4D-CT has enabled us to explicitly address the issue of target volume motion for individual patients. In doing so, we no longer have to rely upon population-based data and margin expansions (11, 12).

The delivery of radiation therapy follows a basic workflow:

- 1) Clinical Consultation;
- 2) Treatment Simulation;
- 3) Treatment Planning;
- 4) Treatment Verification and Delivery.

The process starts with a clinical consultation between the patient and his or her doctor. If it is determined that radiation therapy is the preferred treatment option, a treatment simulation is performed. During treatment simulation, the aim is to acquire images to guide target localization and setup. The patient is ideally simulated in a position that mimics the eventual treatment delivery setup. One method of simulation is performed with a computed tomography (CT) scanner; in cases for which respiratory-induced motion is a concern, a 4D-CT scan may be performed. One situation for which target mobility is a primary concern is when radiation dose is to be delivered to a lung tumor. With information from the 4D-CT, one can better understand how a lung tumor moves during breathing. Based on the images that are acquired during treatment simulation, treatment planning is performed. During the treatment planning phase, targets and normal tissue structures are defined, and radiation beams are virtually placed. The purpose of the treatment planning process is to virtually determine an appropriate means of delivering a prescribed dose to the target. The treatment plan that is created during the planning process contains detailed instructions on how to set up the patient and

how to apply the dose. After a verification process the radiation dose is delivered, following the treatment instructions within the treatment plan.

### **2.1.2      *Basic System Components for 4D-CT***

Three basic components are required to perform a 4D-CT scan: 1) CT scanner; 2) respiratory surrogate; and 3) image processing workstation. The CT scanner is used to acquire projection data over the extent of the volume of interest. During the acquisition of CT data, patient respiration is monitored and recorded with the respiratory surrogate. The respiratory surrogate can come in different forms including an external tracking mechanism, a bellows system, or a spirometer. The goal of each of these methods is to track a physiological change that can be correlated to the respiratory motion. Projection data from the CT scanner and respiratory information from the surrogate are combined using a processing station to create a collection of images that represents different stages of the breathing process. In this collection of images, called the 4D-CT image set, we can visualize how a particular lung tumor moves during respiration.

### **2.1.3      *Cine and Low-Pitch Helical 4D-CT Acquisitions***

There are three primary types of CT image acquisition that are currently clinically utilized:

- Axial Acquisition
- Cine Acquisition
- Helical Acquisition

In an axial acquisition, image data are acquired while the patient bed is stationary. Data are acquired for one gantry rotation and then the table translates to a spatially contiguous location along the cranio-caudal direction. The process of data acquisition and table translation continues until the entire volume of interest is scanned. For each gantry rotation, a CT image (or multiple images for multi-slice CT) is reconstructed.

Performing a cine CT acquisition is conceptually similar to an axial acquisition; however, multiple tube rotations of data are acquired at a single spatial location prior to table translation. Acquiring multiple tube rotations of data over time offers the ability to reconstruct images that represent different time points during the acquisition. When acquiring a cine CT scan, two parameters are available for modification. The cine *duration* determines the amount of time that data will be collected per bed position. The cine *interval* determines the frequency at which images will be generated from the acquired cine CT data.

Figure 1 offers a graphical representation of axial and cine CT acquisitions. The temporal window of data required to create an image is represented by the displayed 'I-beam' shape, and its duration is equal to the tube rotation time. The top portion of the figure shows that an axial acquisition consists of one tube rotation of projection data followed by a table translation. For a cine CT acquisition, shown at the center of Figure 1, data is collected at the same geometric location for multiple tube rotations, followed by table translation. In the example, the cine interval is equal to the x-ray tube rotation time; images are reconstructed adjacent to one another in time, with no temporal overlap. The bottom portion of Figure 1 shows a schematic of a cine CT acquisition with temporal overlap. In the graphic, the cine interval (0.25 s) is set to half of the x-ray tube rotation time (0.5 s). Images are reconstructed from the CT sinogram data in such a way that each image shares half of its data with the image immediately preceding and half of its data with image immediately following it. A shorter cine interval is indicative of more sharing of the data between consecutive CT image reconstructions.

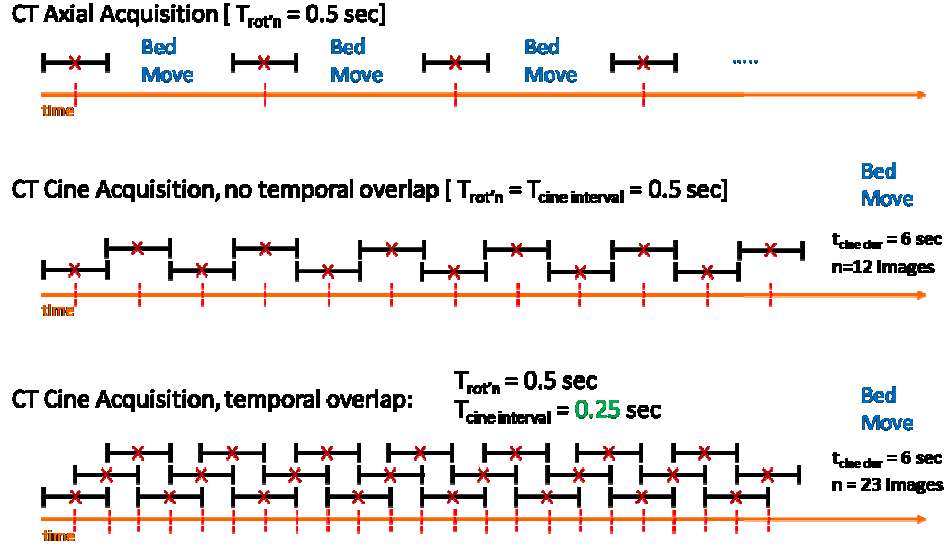


**Figure 1: Schematic of axial and cine image acquisition.**

Graphical representation of (Top) axial acquisition, with one tube rotation creating an image followed by bed translation, (Middle) cine CT acquisition with a six second cine duration followed by bed translation and no temporal overlap of images, and (Bottom) cine CT acquisition with a six second cine duration followed by bed translation and temporal overlap of images.

With a helical acquisition, the rotating x-ray tube is acquiring data while the bed is continually moving at some linear speed, typically described in table distance traveled per tube rotation (mm/rot). Consequently, the data are acquired in a helical trajectory around the patient (25). The relationship between bed motion, tube rotation, and nominal radiation beam width is described by the term *pitch* ( $P$ ), and is calculated as follows:

$$P = \frac{\text{Bed Translation per } 360^\circ \text{ Gantry Rotation [mm/rot]}}{\text{Nominal Radiation Beam Width [mm]}}$$

As the pitch increases, the scan time for a given volume of interest decreases. Because of the translation of the patient during acquisition, a helical acquisition relies upon data interpolation to create a planar image set.

With regard to 4D-CT acquisitions, current scanning techniques fall in to one of two general categories: 1) cine CT acquisition with *image* sorting; or 2) low-pitch helical acquisition with



*sinogram* binning. In image sorting with cine CT, images are acquired with the table stationary for a set time interval, as described above. The cine CT images that are reconstructed are associated with the respiratory waveform, and a subset of images is selected that correspond to different snapshots of the tumor motion during respiration.

In sinogram binning with a low-pitch helical acquisition, the selection of target respiratory states is made prior to image reconstruction. The pitch during a 4D-CT low-pitch helical acquisition is much smaller than is typically utilized in a clinical helical acquisition (commonly clinical range between 0.75 - 1.5), and typically ranges between 0.05 and 0.15 (17). For the purposes of CT data acquisition, the pitch must be low enough so as to capture at least one full breath cycle at each location. A longer respiratory cycle necessitates the usage of a lower pitch. Based on the respiratory surrogate information, target respiratory states are identified and images are reconstructed using the sinogram data.

## **2.2 Cine CT Based 4D-CT with Varian Real-time Position Management System**

In this study, the method of acquisition that was used was a cine CT acquisition with retrospective sorting. The respiratory surrogate was a commercially available monitoring device (Real-time Position Monitor [RPM] system v. 1.6, Varian, Palo Alto, CA). The monitoring system uses a block with two infrared (IR) reflective dots placed on the patient's abdomen in combination with a tracking IR camera. As the patient breathes during the acquisition, the block rises/falls and video data is captured by the infrared camera. The video data are analyzed on an accompanying RPM processing station. The main functions of the RPM processing station are:

- 1) Amplitude tracking and measurement of block location with time;
- 2) Detection of x-ray tube status (beam-on or beam-off);
- 3) Identification of end-inspiration (EI or 0%) points;
- 4) Calculation of numerical phase.

The block amplitude is sampled at a frequency of 30 Hz (i.e. one measurement every 33.3 msec). With each sample, the block amplitude and x-ray tube state (beam-on or beam-off) are determined. Additionally, the identification of each end-inspiration (EI or 0%) is performed, and the numerical *phase* is calculated for each data sample. There are two stages of EI identification and associated phase calculation: 1) active identification/calculation during the acquisition of respiratory data using predictive filtering; 2) post-processing identification/calculation using the entirety of respiratory data. In this study, the 4D-CT sorting was performed using the post-processed data files. The numerical representation of breathing phase is generally expressed in one of two ways – as a floating point value varying between 0 and  $2\pi$  or as a percent value varying between 0% and 100%. In both cases, the 0 or 0% phase corresponds to the end-inspiration (EI) point. Between each subsequent identified EI point, numerical phase is calculated assuming a linear phase progression. Figure 2 shows a simulated sinusoidal respiratory waveform with the identified end-inspiration points and associated phase calculation. The figure depicts the fact that phase values between the EI points are linearly interpolated from 0 to  $2\pi$  or from 0% to 100%.

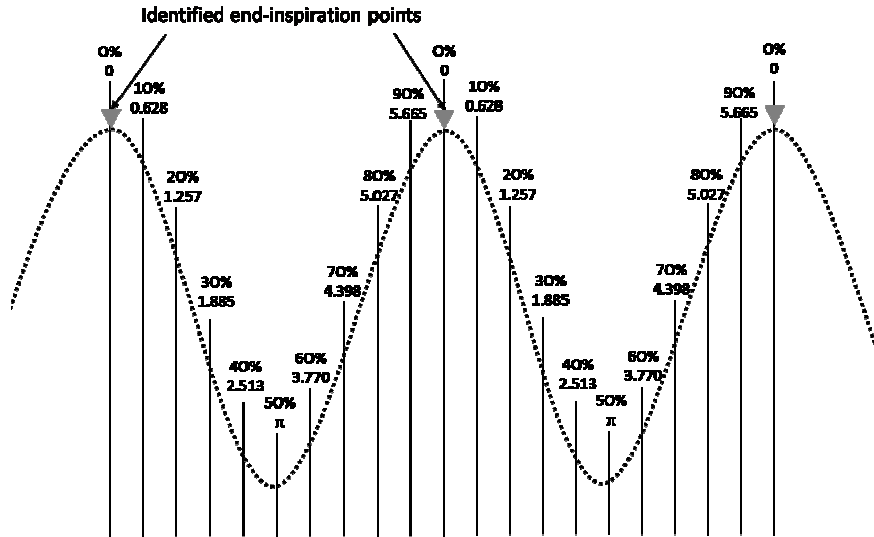


**Figure 2: Calculation of numerical phase with respiratory surrogate.**

Simulated sinusoidal respiratory waveform along with sample calculation of numerical phase for multiple breath cycles. The respiratory surrogate system identifies the end-inspiration points (EI) and assigns a numerical phase for each data sample, assuming a linear phase angle progression.

Figure 3 shows three pieces of hardware that can be used to perform cine CT based 4D-CT acquisitions. While the respiratory motion is recorded by the respiratory monitoring device, CT data are acquired over the volume of interest using a cine CT acquisition. Once cine CT acquisition is complete, the images are sent to the image processing station along with the respiratory data file from the RPM system.

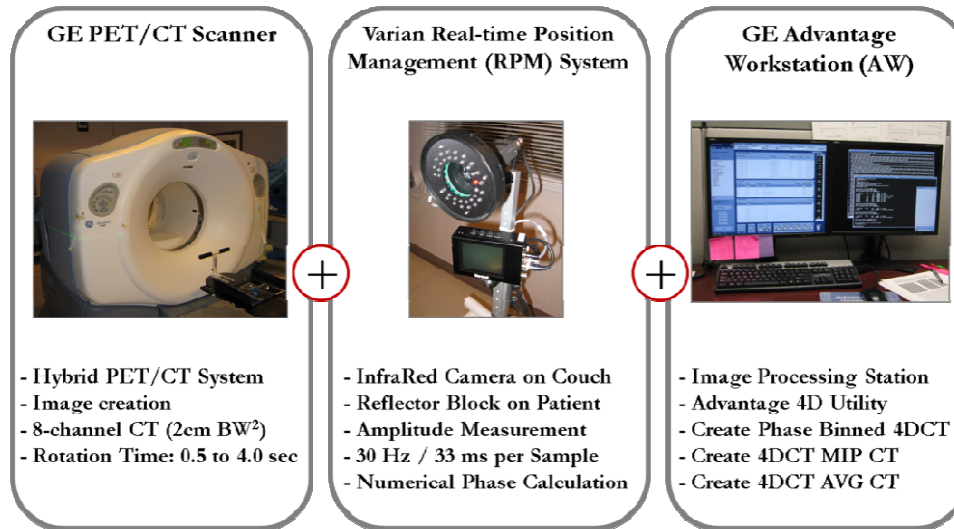


**Figure 3: Hardware for cine CT based 4D-CT with Varian RPM.**

Photos of sample hardware associated with cine-based 4D-CT with real-time position management (RPM) respiratory surrogate. Left, GE PET/CT scanner used for image data acquisition. Middle, Varian RPM consisting of reflective block placed on patient abdomen and infrared camera used to collect respiratory information. Right, processing station used to perform 4D-CT sorting and to generate MIP and RACT images.

Once on the processing station, the 4D-CT sorting process may be performed (the processing station may be independent or incorporated into the CT scanner hardware). The time scales of the respiratory surrogate and the cine CT images are aligned. Then, cine CT images that were generated during the CT data acquisition are associated with the calculated numerical phase values within the respiratory data file. Images at each bed position are selected that best represent different target phases of the breath cycle. Commonly, cine CT images are sorted in to 10 different phase bins, with target phases of 0% to 90%, in steps of 10% phase angle. The final output is a group of 3D image sets (each set representing a different phase of the breath cycle), collectively called the 4D-CT image set.

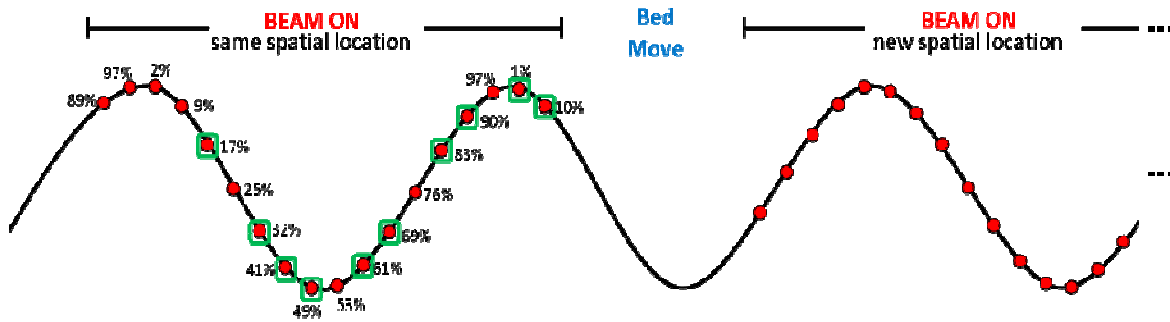


**Figure 4: 4D-CT phase-binning selection process.**

With 4D-CT phase-binning, each cine CT image that is created is associated with the numerical phase calculated within the respiratory data file. For each bed location, a representative image is selected that most closely represents target phases. In this example, target phases are 0% to 90% in steps of 10% phase angle. The selection process is repeated for each bed position, resulting in 10 different image sets, each representing a different breathing phase.

### **2.2.1 Components of Varian RPM Data File**

The primary output of the Varian RPM system is a data file containing measurement information of the patient's breathing pattern. Within the data file, each line of data is associated with a time stamp, given in milli-seconds and generated at a frequency of 30 Hz. The associated amplitude and beam status (TTLIN: equals '1' for beam-off and '0' for beam-on) are documented for each sample. The MARK column contains information defining the end-inspiration (EI or 0%) and end-expiration points (EE or 50%) – a value of 'Z' indicates an EI point and a value of 'P' indicates an EE point. Based on those identified EI and EE points, the numerical *phase* is calculated for each sample. As discussed in Section 2.2, the PHASE is a value between 0 and  $2\pi$  and is meant to represent the different stages of the breathing cycle. Finally, the VALIDFLAG column allows the user to define portions of the respiratory trace as valid (value equals '0') or invalid (value equals <neg>). By setting a range of the VALIDFLAG values to a negative numerical value, images created during that time will not be selected during 4D-CT sorting process. Table 1 below shows the contents of the respiratory data file.

**Table 1: Contents of respiratory monitoring RPM data file.**

Sample content within the data file, each line of data represents a data sample taken by the respiratory surrogate at 30 Hz. Included in the file is the timestamp, amplitude measurement, calculated phase, the valid flag, the x-ray beam status (beam-on or beam-off) indicator, and the identified end-inspiration points.

AMPLITUDE	PHASE	TIMESTAMP	VALID FLAG	TTLIN	MARK	TTLOUT
4.8796	6.2118	115360	0	1		0
4.8641	0	115393	0	1	Z	0
4.8609	0.0628	115426	0	1		0
4.8613	0.1257	115460	0	1		0
4.8631	0.1885	115493	0	1		0
4.872	0.2513	115526	0	1		0
4.8802	0.3142	115560	0	1		0
4.9199	0.377	115594	0	1		0
4.9564	0.4398	115627	0	1		0
5.0072	0.5027	115660	0	1		0
5.061	0.5655	115694	0	1		0
5.1351	0.6283	115727	0	1		0
5.2068	0.6912	115760	0	1		0
5.3081	0.754	115794	0	1		0
5.3952	0.8168	115827	0	1		0
5.4968	0.8796	115861	0	1		0
5.5909	0.9425	115894	0	0		1
5.6888	1.0053	115927	0	0		1
Direct Measure of Block Amplitude	Calculated Phase 0 - $2\pi$	Timestamp in msec	Valid Flag: Active = 0 Invalid = <->	Beam Status Indicator: ON = 0 OFF = 1	Identified Peak/Valley: End Insp = 'Z' End Exp = 'P'	

## 2.3 External Beam Radiation Therapy and 4D-CT

EBRT to the thorax is typically delivered over a number of days by dividing the dose into multiple fractions. The goal of radiation therapy is to deliver dose to a target, while simultaneously sparing dose to normal tissue (26). With any treatment strategy, the effects on the tumor and on the normal tissue must be considered. The therapeutic ratio has been defined as a metric to compare the relationship between tumor treatment response and toxicity to normal tissue – a good therapeutic ratio indicates a favorable balance between tumor damage and damage to normal tissue (27). A fractionation approach is meant to result in an improved therapeutic ratio by taking advantage of various biological factors. Biological factors include a complex interplay between the radiosensitivity

of tissue cells, the repair of radiation damage, cell repopulation with time, the redistribution of proliferating cells, and reoxygenation of hypoxic cells (26).

With the aim of improving the therapeutic ratio, recent studies have shown that the usage of a hypofractionation scheme is beneficial (1). One such hypofractionation scheme that is the focus of this study is stereotactic body radiation therapy (SBRT). In SBRT, a higher dose per fraction is used for fewer treatment days. The total delivered dose is on the same order as conventional fractionation. For example, a conventional fractionation method may deliver 2.0 Gy/fx for 25 fractions (total dose of 50 Gy), whereas an SBRT may deliver 12.5 Gy/fx for 4 fractions (total dose of 50 Gy). Because of the use of a smaller number of fractions and a larger dose per fraction, the importance of proper target localization increases. Figure 5 shows

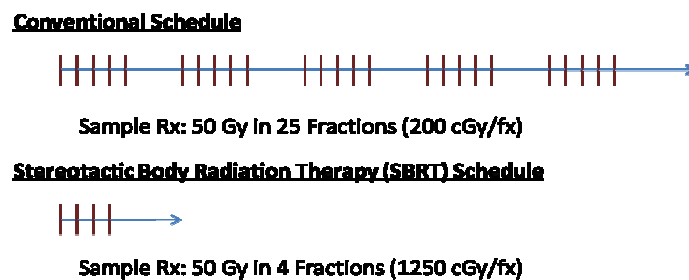


**Figure 5: Conventional and stereotactic dose delivery schedules.**

Schematic of dose delivery schedules for a conventional schedule (top) and for a stereotactic schedule (bottom). Notice that the stereotactic schedule utilizes a hypofractionation scheme, which utilizes fewer fractions with larger daily dose per fraction.

### **2.3.1 *Maximum-Intensity Projection Images for Target Delineation***

To assess target location and motion, 4D-CT can be used, and one image set that can be developed is the MIP. The property of the MIP that is useful in treatment planning is that it identifies the volume encompassing the geometric location of the lung tumor at any point throughout the respiratory cycle. Knowledge of how and to where a tumor moves with respiration is important because it is different for all patients (13). Dose is delivered using multiple fields that encapsulate the

entire tumor motion envelope. This ensures that the tumor resides within the treatment field at all times, but also leads to the irradiation of more normal tissue for tumors that have a large motion.

There are situations for which the tumor location information within a MIP may be obscured. One situation that has been previously cited is that a tumor at the base of the lung may be over-written by the tissue of the diaphragm or liver. The MIP consists of a pixel-by-pixel maximum CT number. Soft tissues have similar densities, and if the paths of motion for the tumor and the diaphragm/liver overlap, a loss of contrast may occur. Figure 6 shows a clinical example of a MIP with a tumor motion path that was over-written with tissue in the diaphragm. The loss of contrast on the posterior edge of the tumor border can be seen in image b), which can be problematic when defining the iGTV; however, methods have been developed to deal with this issue, such as the usage of other image sets or the creation of modified image sets (28).

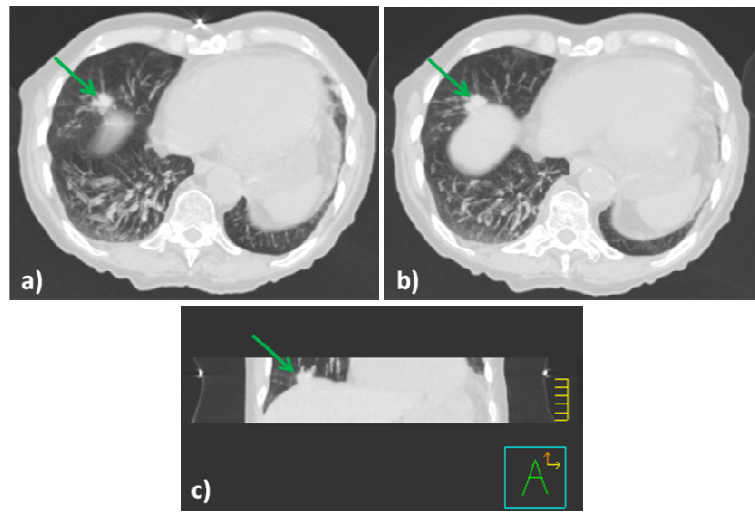


**Figure 6: Clinical example of diaphragm over-writing tumor in MIP.**

Clinical example showing a lung tumor near the base of the lung in a MIP. Images a) and b) show axial CT images at different slice locations near the tumor/diaphragm interface. In a), the tumor boundary can be visualized. In b), which was taken from a more inferior slice, the tumor boundary is more obscured by the high density diaphragm. The coronal view shown in c) shows that the superior portion of the tumor can be seen, but the inferior portion is clipped by the diaphragm.



### 2.3.2 *Current Clinical Protocol for Cine Based 4D-CT*

When a patient arrives to have a 4D-CT simulation performed, he or she is positioned on the couch in the treatment position. Ideally, during a 4D-CT scan, the patient should breathe normally, as he or she would during treatment delivery. Gross movement or breathing aberrations such as coughing or deep inspiration represent a departure from a normal state and are discouraged. The RPM block is taped to the anterior abdomen of the patient, and visualization of the block with the infrared camera is confirmed.

The standard 4D-CT scan consists of a collection of image acquisitions. The process begins with the acquisition of a *scout* or *topogram*. During a scout acquisition, the CT tube is stationary, and the patient sweeps through the radiation beam while maintaining deep inspiration. The resultant image looks like a planar radiograph, and is used for an initial assessment of patient positioning. Also, the scout image serves as a roadmap to determine the scan extent for the upcoming CT image acquisitions. The scout is typically acquired during deep inspiration so that the CT technologist can have an estimate of the largest lung extent in the superior-inferior (SI) direction.

The second scan is a helical acquisition taken while the patient is breathing. This free breathing (FB) scan typically covers from the mandible down to the base of the liver. The 3D image set from this scan will show the target volume and can be used for dose calculation and serves as a backup to the 4D-CT process. Since the patient is breathing during the acquisition, one can expect that motion artifact may be visible in some portions of the scan.

The third scan is a cine CT acquisition of the thorax. The images created from this scan are utilized in the 4D-CT sorting process. To determine the cine duration, the respiratory waveform is monitored to determine the patient's respiration rate. To ensure the capture of an entire breath cycle at each bed position, the cine duration is set to the observed respiration rate plus one second. The cine interval is set based on a reconstruction engine limitation that allows the reconstruction of a maximum of 3000 images within a single series. Section 2.1.3 showed that decreasing the cine interval increases the number of reconstructed images. The cine interval is therefore a function of

patient-specific parameters including the scan extent, the cine duration, as well as the inherent hardware limitations. A typical cine interval ranges between 0.25 s and 0.35 s; in general, a smaller cine interval leads to more images and better phase-matching during the 4D-CT sorting process.

Once the cine CT acquisition is complete, the respiratory trace is inspected to ensure regular breathing throughout the cine CT data collection. If it is determined that the patient breathing was adequately consistent, images are pushed over to the image processing station. Likewise, the respiratory data file is pushed to the processing station. On the processing station, the 4D-CT sorting is executed, as described in Section 2.2. Other image sets are created on the processing station for various uses throughout the treatment planning process. The final available image sets include:

- CT Scout(s)
- Free-breathing CT Image Set
- Cine CT Image Set
- Phase-binned 4D-CT Sorted Image Sets (10 series, 0% / 10% / ... / 80% / 90%)
- Maximum Intensity Projection (MIP) CT Image Set
- Respiratory Averaged CT (RACT or AVG CT)

The new image sets that were created as a result of the 4D-CT sorting process include the sorted 4D-CT image sets, the MIP, and the RACT. The 4D-CT image set consists of 10 phase-binned image sets that depict the patient at different phases of the respiratory cycle. For a given slice location visualizing the lung tumor, sequentially flipping through the sorted 4D-CT phases will depict the motion of the tumor as the patient breathes. The MIP image that is created consists of the pixel-by-pixel maximum value over any of the 4D-CT image sets. Ideally, the MIP should highlight the region of volume that the moving lung tumor occupies at any point during the patient's respiration. Practically, this can help identify the volume encompassing the motion envelope of the tumor, or internal gross target volume (iGTV). The iGTV is the motion envelope of the gross target volume (GTV); unlike the other target volume definitions, iGTV was defined at our institution to describe the utilization of image data from the 4D-CT process. Finally, the RACT image set is the arithmetic

average of the 4D-CT image sets. Because of the averaging process, RACT images tend to show a blurred appearance of moving objects. In the case of lung tumors, the apparent tumor density in a pixel shown in the RACT is related to the time interval for which the tumor is present in that location. Because of the time average properties of the RACT, it is often the image set on which dose calculations are performed.

### 2.3.3 4D-CT and Thoracic Treatment Planning

The images that are created from the 4D-CT process are sent to a treatment planning system (TPS). Within a treatment planning system, virtual beams are placed with the goal of delivering a prescribed dose. To define the target, the user can use the available MIP. Additionally, the radiation oncologist or dosimetrist can refer to the 4D-CT phase images, RACT images, and FB images. Figure 7 shows the general workflow of how image sets that are created during simulation are used during the treatment planning phase.

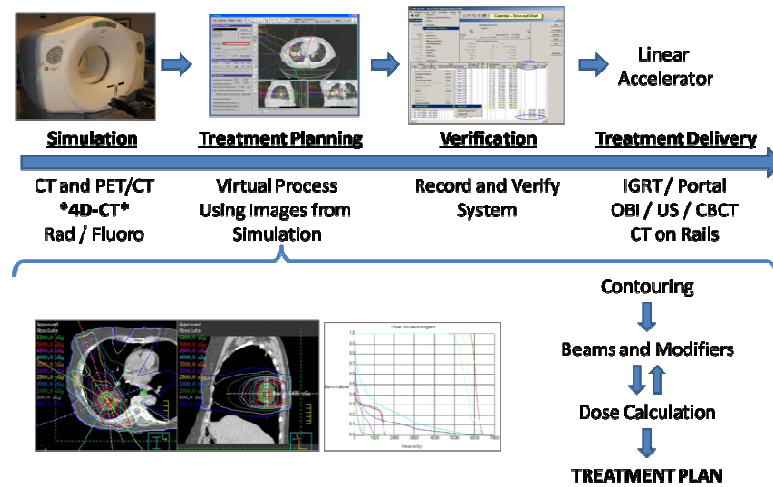


**Figure 7: Radiation therapy general workflow.**

Images acquired during a simulation (4D-CT, in our case) are sent to a treatment planning system for identification of the target and surrounding structures, placement of virtual beams/modifiers, and for dose calculation. The final treatment plan goes through a verification process, and instructions are used during the treatment delivery.

Once the target is identified and contoured, additional margins are added to account for various biological and setup conditions. The International Commission on Radiation Units and Measures (ICRU) has produced a collection of reports defining what volumetric expansions to apply to a target volume (11, 12). ICRU 62 defines the gross target volume (GTV) as the demonstrable volume and extent of the tumor. A margin is added to the GTV to account for microscopic extension of disease that is not visible on the imaging modality, and is called the clinical target volume (CTV). The internal target volume (ITV) includes the CTV plus an internal margin which aims to account for expected physiologic motion. The internal margin is a generic expansion that was generated based on population-based data. A final expansion is applied to the ITV, and is called the planning target volume (PTV). The margins up to the PTV are added to account for setup uncertainty and to ensure that the prescribed dose is delivered to the CTV (12). Figure 8 shows a graphical representation of the volume expansions described in ICRU 62.

The definitions of target volumes within ICRU 62 were published in 1999, prior to the clinical implementation of 4D-CT. 4D-CT offered the ability to explicitly account for target motion for each individual patient, instead of relying on population based expansions, such as in the case of internal margins. With the new abilities offered by 4D-CT, our institution developed a method of volume definition that is founded on the ICRU definitions. The internal gross target volume (iGTV) was defined as the volume encompassing the motion envelope of the moving GTV. The most direct method of defining this volume is through the utilization of a MIP that can be generated from a 4D-CT scan. A margin is added to the iGTV to account for subclinical disease, resulting in the ITV. Another margin is added to the ITV to account for setup uncertainty and to ensure delivery of the prescribed dose to the ITV, and is called the PTV. Implementing these volume definitions leads to an individualized assessment of tumor motion. Figure 8 also shows the process of margin expansion as defined by our institution. It shows that the volume encompassing the moving GTV is captured by the iGTV. Also, it displays the additional margins are added to the iGTV to account for biological

and setup conditions. In this project, our focus was primarily on SBRT, and additional margins are performed somewhat differently – the PTV is generated directly from a margin added to the iGTV.

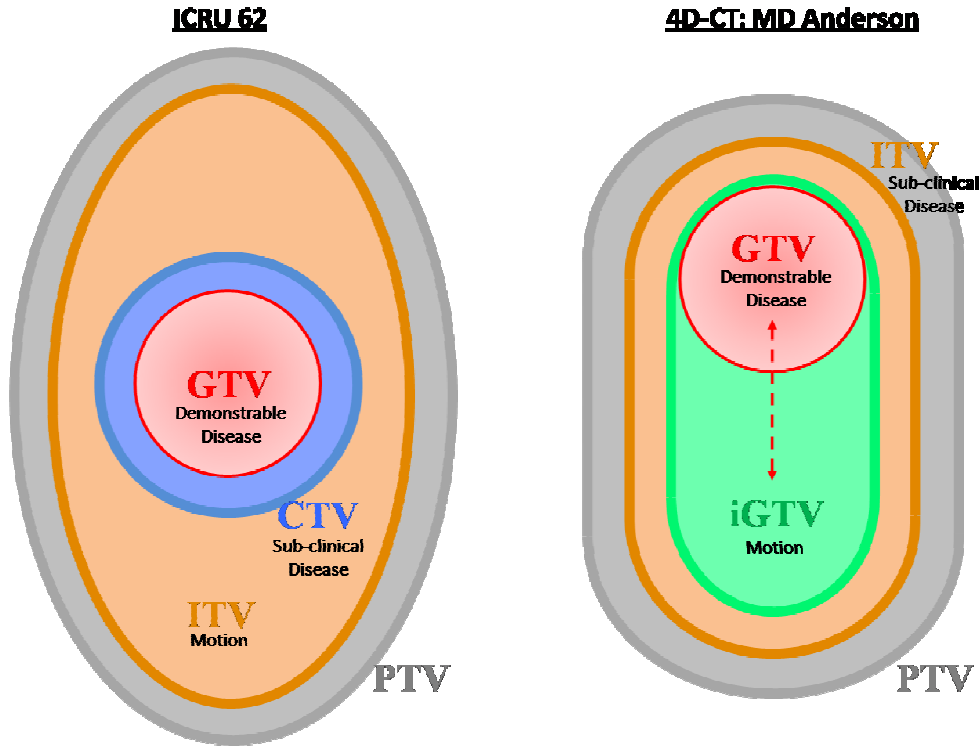


**Figure 8: Definition of margin expansions to gross target volume (GTV).**

Graphical representation of margin expansions that define different target volumes used in radiation therapy. Left, the demonstrable GTV is defined by an imaging modality. Simulated margins expansions as defined in ICRU 62, including accounting for subclinical disease (CTV), expected physiologic motion (ITV) and setup uncertainty (PTV). Right, the definitions of target volume using the methodology generated at our institution, using the new abilities offered by 4D-CT.

### **3. SPECIFIC AIM 1: PATIENT SELECTION AND IMAGE PROCESSING**

#### **3.1 Objectives**

In specific aim 1, our goal was to select a population of patients for which we could develop MIP data sets using various methodologies. For the selected patients, we used a collection of different software to produce MIP image sets using four different methods. The primary focus was on patients that had prior 4D-CT scans with lung tumors (NSCLC) that displayed respiratory-induced motion of at least 1 cm. Tumors with high motion amplitudes served to amplify the differences between each MIP image set. The careful selection of patients allowed us to proceed to further stages of this study to quantitatively compare the resultant iGTV in each MIP data set.

#### **3.2 Materials and Methods**

This study was approved by our institutional review board. Patients eligible for this study were those who had previously undergone thoracic 4D-CT scans at our institution between 2005 and 2010 for the treatment of non-small-cell lung cancer (NSCLC). Patients were candidates for SBRT and were chosen only if the lung tumor exhibited respiratory-induced motion of at least 1 cm and had a simple structure and clear boundaries to facilitate automatic contouring. The 4D-CT workflow used at our institution on our 8-slice PET/CT scanner (Discovery ST; GE Healthcare, Waukesha, WI) consists of a breath-hold CT scout to determine maximum lung extent, followed by a free-breathing helical CT of the chest and abdomen, and then a cine CT acquisition of the chest. The acquisition and usage of cine CT images in 4D-CT has been extensively described (15, 29). In short, a cine scan generates multiple images at a single bed position through the acquisition of projection data over a period of time equal to at least one respiratory cycle. The patient bed is then incremented a distance equal to the nominal radiation beam width so that image data is contiguous in space over the entire scan extent. For our patients, cine scan images were acquired at 120 kVp, 100 mA, 8 x 2.5 mm detector configuration, 2.5 mm image thickness, and a 0.5 s/revolution tube rotation time. The cine

duration was set to approximately one breath cycle plus 1 s, and images were reconstructed at a cine reconstruction interval, typically 0.25 s (30).

During the cine scan, respiratory motion was monitored and recorded by tracking the patient's anterior abdominal surface with a commercial respiratory monitoring device (Real-time Position Management (RPM) system, Varian, Palo Alto, CA). The monitoring system uses a reflective block placed on the patient's abdomen in combination with a tracking infrared camera. Samples of the block amplitude are acquired at 30 Hz and stored in a data file. Within the data file, end-inspiration (EI or 0%) points are identified on the respiratory trace; the respiratory phase is then calculated between subsequent EI points, assuming a linear phase progression. Next, the cine images that have been created are temporally correlated with the respiratory data file, and the best-fit images are selected to meet a set of target parameters, thereby creating the 4D-CT image set.

In this study, we examined four different MIP image sets: (1) phase-binned (PB) based on retrospective phase calculations; (2) phase-corrected phase-binned (PC-PB) based on motion extrema; (3) amplitude-binned (AB); and (4) cine CT built from all available images. We used previously-developed sorting software to execute the different 4D-CT sorting methods (that is, the first three methods listed here) and to generate all four of the MIP image data sets (20). In the remainder of this paper, subscripts refer to the method employed to create a particular data set.

Method (1) utilizes the respiratory data file and associated phase calculations to perform the PB sorting. Within the respiratory data file, the 50% point is temporally centered between the identified end-inspiration (EI) points; no attempt is made to correlate the 50% point as the end-expiration (EE) or minimum measured RPM amplitude. To address this, a "PhaseCorrect" (PC) software was previously developed to retrospectively identify the EI and EE points as the respective maximum and minimum amplitudes, and then to recalculate the numerical phase between each identified point (0% - 50% and 50% - 100%), resulting in a modified or PC respiratory data file (17). For method (2), a phase-based sorting method is applied using the PC phase calculations. Since the durations of expiration and inspiration are not typically equal when defining the EE as the minimum

amplitude, we expected that images selected based on a PC respiratory file would be different from images selected by the un-modified respiratory file, as in the PB method. For both PB and PC-PB methods, images were directed into 10 bins, with target phases of 0% - 90% in steps of 10% phase angle.

The  $MIP_{4D-CT,AB}$  in method (3) is generated based on an AB methodology (2, 20); instead of sorting the images based on the calculated respiratory phase, images are sorted based on the measured amplitude of the respiratory signal. The implementation of AB identifies the images created at the maximum and minimum amplitude for each bed position. From those extreme amplitudes, we define equally spaced target amplitudes for inspiration and for expiration. This method is meant to force the selection of the images correlated to the most extreme amplitude positions, and then to select images at equal amplitude increments during inspiration and expiration. There are 10 bins defined for each bed position, and 10 images selected for each slice location. Figure 9 offers a graphical representation of the 4D-CT selection process for each of the three sorting methods applied to the same input data. Note that method (4), yielding  $MIP_{CINE}$ , uses all available cine CT images.



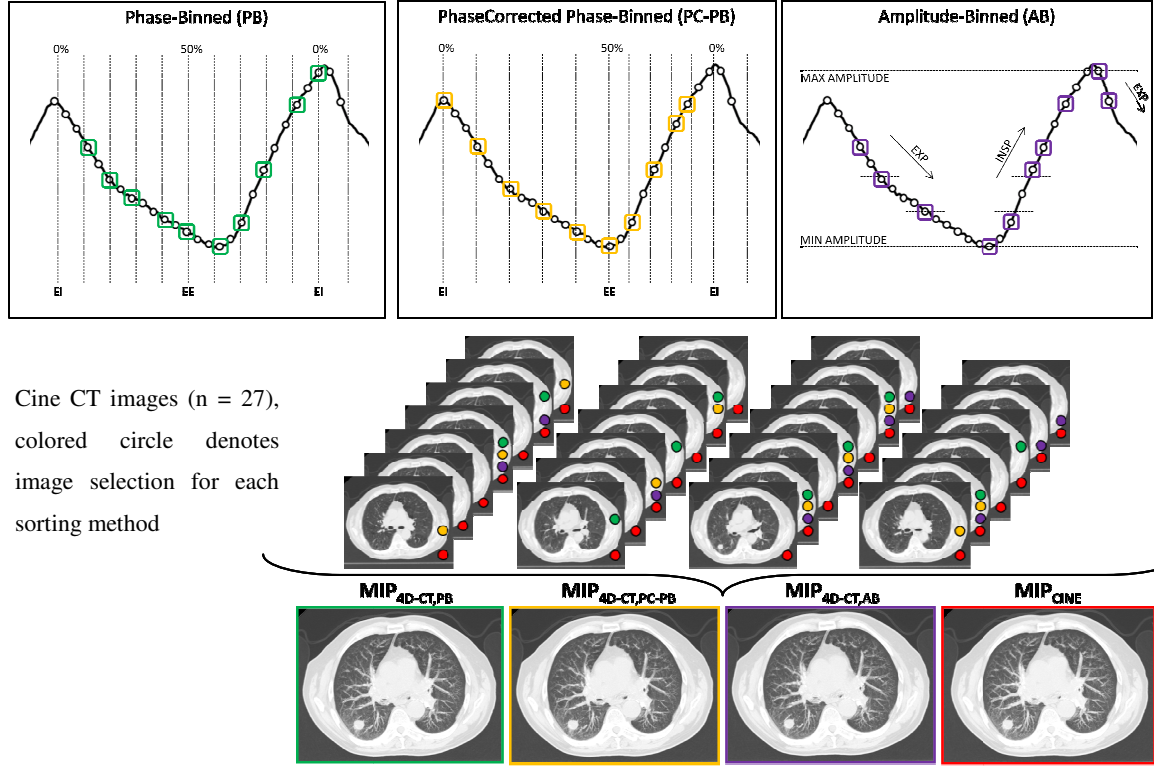


**Figure 9: MIP images generated in this study.**

MIP images generated from one of three 4D-CT sorting processes (PB, PC-PB, AB) or from use of all 27 cine CT images. Top, the respiratory signal at a single bed position on a representative patient case showing that the same input will lead to the selection of a different distribution of 10 images for each different sorting method (bottom). Each of the three MIP<sub>4D-CT</sub> image sets is generated from the selected images.

### **3.2.1      *Patient Selection Criterion***

The primary clinical motivation for a 4D-CT scan is to assess motion of lung tumors or of tumors within the gastro-intestinal system (i.e. esophagus, liver) for the purposes of treatment planning. Since 2004, thousands of 4D-CT scans have been performed at our institution. All of the image data and respiratory surrogate data files are archived and were available for this study. In our clinic, we have access to equipment to perform 4D-CT via image sorting or sinogram binning. In this study, we focused on patients that had undergone thoracic 4D-CT scans on our 8-slice PET/CT scanner that acquires cine CT images and performs 4D-CT image sorting. Patients in this study presented with non-small cell lung cancer (NSCLC) and were candidates for SBRT. Also, patients were selected only if the lung tumor exhibited respiratory-induced motion of at least 1 cm and had a simple structure and clear boundaries to facilitate automatic contouring. For each patient, we measured the tumor displacement on a standard three-plane view (anterior-posterior/superior-inferior/left-right) of the clinical PB 4D-CT and calculated the quadrature sum to find the total tumor excursion.

### **3.2.2      *Development of Maximum Intensity Projection Images – Sorting Software***

To create the maximum intensity projection images in this study, we used a previously developed program to perform the 4D-CT sorting. Figure 10 shows graphically how the sorting software fits into the data processing workflow. It shows on the left the clinical hardware used to acquire 4D-CT information, including the CT scanner, the respiratory surrogate, and the processing station. However, instead of using the processing station to perform the 4D-CT sorting and the image reconstruction, the RPM data file from the respiratory surrogate and the cine CT images from the CT scanner are both transferred to a local PC for processing. After image sorting and reconstruction are complete, the new image sets are pushed back to the GE AW, and then pushed to a treatment planning system.

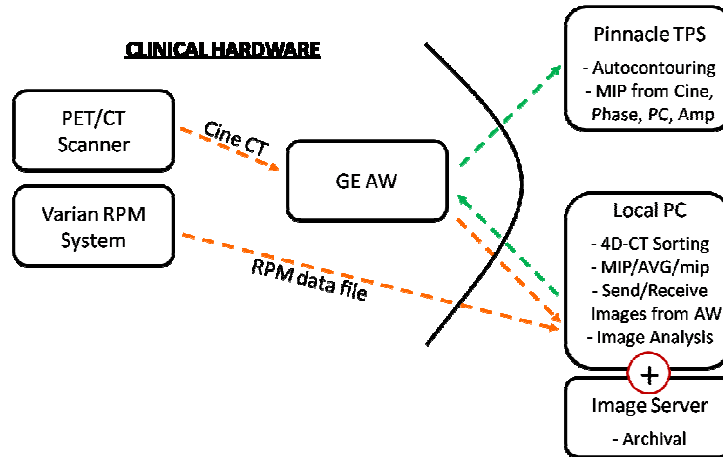


**Figure 10: Project workflow for performing data processing.**

Schematic showing the data workflow for data processing associated with this project. Data from the three clinical hardware components on the left are redirected to a local PC where sorting and image reconstruction occurs. Images are redirected to the image processing station (GE AW) and then pushed to the treatment planning software (Pinnacle) for automatic contouring.

Figure 11 shows the graphical user interface of the sorting software. There are three main functions of the software that allow it to be integrated into the processing workflow. First, the software *retrieves* images from the GE AW. On the GE AW, the user highlights the image series of interest (in our case, the cine CT image series), and then clicks ‘receiving’ on the sorting software. Images are then imported into a defined folder location on the local computer. Second, the software performs the *sorting* and image generation function. Three options are available: 1) Phase-sorting; 2) Amplitude-sorting; and 3) AVG/MIP/mip. The phase-sorting option executes the phase-based binning based on the input respiratory data file; therefore, the user can perform PB or PC-PB by changing the respiratory file as desired. The amplitude-sorting option executes an amplitude-binning methodology using the amplitude measurements within the respiratory data file. In both cases (phase-binning or amplitude-binning), once the 4D-CT sorting process has completed, MIP, RACT, and mip (minimum-intensity projection) image sets are generated from the selected 4D-CT image set. The mip image set is created in a similar fashion to the MIP, only it is generated using a pixel-by-pixel

*minimum* CT number value. The third option, ‘AVG/MIP/mip,’ creates a MIP, RACT, and mip using the entire collection of cine CT images. The final function of the software is to *send* the images that were created back to the GE AW, where they can then be pushed to a treatment planning system.

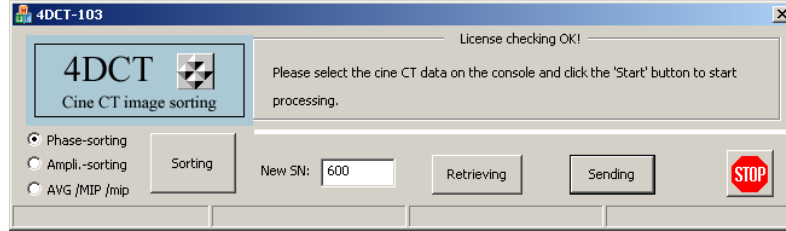


**Figure 11: User interface for 4D-CT sorting and image processing software.**

Snapshot of the user interface of the 4D-CT sorting software shows three main processes - sorting (via phase-binning, via amplitude-binning, or from all cine CT) or sending/retrieving images to/from the image processing station (GE AW). *Sorting program developed by Tinsu Pan, Ph.D. and Xiaojun Sun for usage in reference(20).*

### 3.2.2.1 Implementation of Phase-Binning [PB]

The sorting software executes a PB methodology as described in Section 2.2. During the CT acquisition, the respiratory motion is tracked by a surrogate. The main output from the respiratory surrogate is a data file with tracking information. The data file contains numerical calculations of phase, meant to describe the stage of the breathing process. CT images that are acquired are associated with the respiratory phase within the data file, and a set of best-fit images are selected. In our study, images were directed into 10 different bins, with target phase values of 0% through 90%, in steps of 10% phase. The sorting process builds the 4D-CT image set, which consists of 10 series of images, each series representing a different phase of the breath cycle.

### 3.2.2.2 Implementation of Phase-corrected Phase-Binning [PC-PB]

The PC-PB implantation follows the same general selection process as described for PB; however, the calculation of numerical phase within the respiratory data file is performed differently. Section 2.2 describes the process of phase calculation used within the RPM system respiratory file,

whereby a value between 0 and  $2\pi$  is assigned to each sampling between identified EI points. A problem that has been noted in previous publications is that the identification of the EI is not always exactly at the maximum amplitude value, particularly in data sets from patients exhibiting irregular breathing (20). Also, since the numerical phase is linearly interpolated between the identified EI points without regard to the breathing pattern, image artifact may be more likely to arise if the patient changes breathing cadence during the course of the CT scan. The typical breath cycle for a patient is not symmetric, that is to say that the time for expiration is typically longer than the time for inspiration. What has been previously implemented is a program that retroactively modifies the respiratory data file generated from the RPM system. The program correctly identifies the 0% point as the maximum measured amplitude and the 50% point as the minimum amplitude, or EE. Based on the newly defined 0% and 50% points, the numerical phase is recalculated from 0 – 50% and from 50 – 100%, assuming a linear phase angle progression. This process serves two main purposes in that it allows for a more accurate identification of the peak inspiration and that it also forces the EI point to the minimum amplitude. Both processes have exhibited positive results when applied to clinical cases (20).

The process of modifying the respiratory data file in this manner has been termed phase-correcting (PC), and is currently utilized in our clinic in selected cases. Figure 12 shows the user-interface of the PC software. For a selected respiratory data file, the PC software will retrospectively force the 0% and 50% points to the respective maximum and minimum amplitude measurements. The user also has the ability to manually delete or reassign the 0% and 50% points in the event of incorrect identification or irregular breathing patterns.

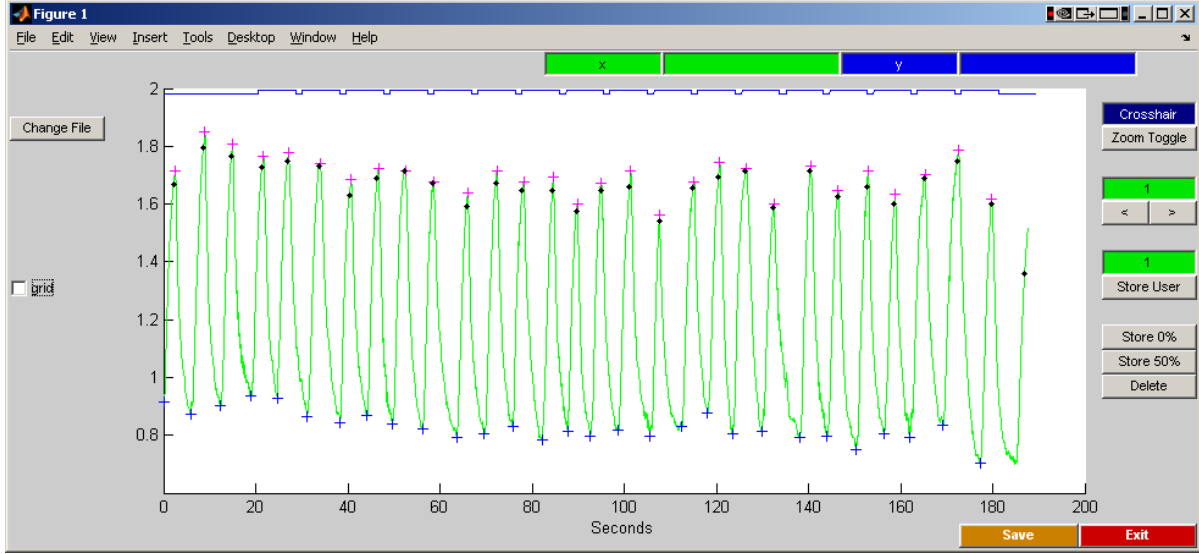


**Figure 12: User interface of phase-correct software.**

This graphic shows the user interface for the PC software modifying an acquired respiratory waveform. EI points within the original data file are displayed as a dark dot. Correctly identified EI points are shown as a pink cross, and the identified minimum amplitude EE are shown as a blue cross. Manual modification of these identified points is possible with the available tools.

An identical phase-based sorting process is then performed with the PC respiratory data file. Each cine CT image is associated with the new numerical phase as calculated within the PC data file, and the best-fit images are selected to represent phases 0% through 90%, in steps of 10% phase angle. Again, the sorting process constitutes the 4D-CT image set.

### 3.2.2.3 *Implementation of Amplitude-Binning [AB]*

The implementation of AB performs sorting based on the amplitude measurements taken from the respiratory data file instead of the calculated numerical phase. Generally speaking, two main methods of AB have been presented in the literature – that based on a global amplitude extrema and that based on local amplitude extrema (2, 3, 14, 31). The method used in this project is based on the localized application of AB process.

As in the PB and PC-PB methods, cine CT images are acquired while the patient respiration is monitored and documented by a respiratory surrogate. Instead of associating the calculated phase, each image is associated with the nearest measured amplitude value. The sorting program also determines and associated the direction of respiration (inspiration or expiration) with each image. At a given bed position, the sorting program identifies the two images associated with the maximum and minimum amplitudes. Then, target amplitudes (during inspiration and expiration) are calculated as evenly spaced values between the identified maximum and minimum amplitude. Figure 13 shows a clinical example of how the AB methodology selects the images during the image sorting process. In the figure, the images at the maximum and minimum measured amplitude are selected. Based on those amplitude values, 8 target amplitudes (4 during inspiration and 4 during expiration) are defined for the bed position, and are equally spaced between the extrema. Every cine CT image is associated with an amplitude and direction (up for inspiration or down for expiration). The best-fit images are selected based on the associated amplitude and direction. The process is repeated for each subsequent bed position, and the 4D-CT data set is generated.

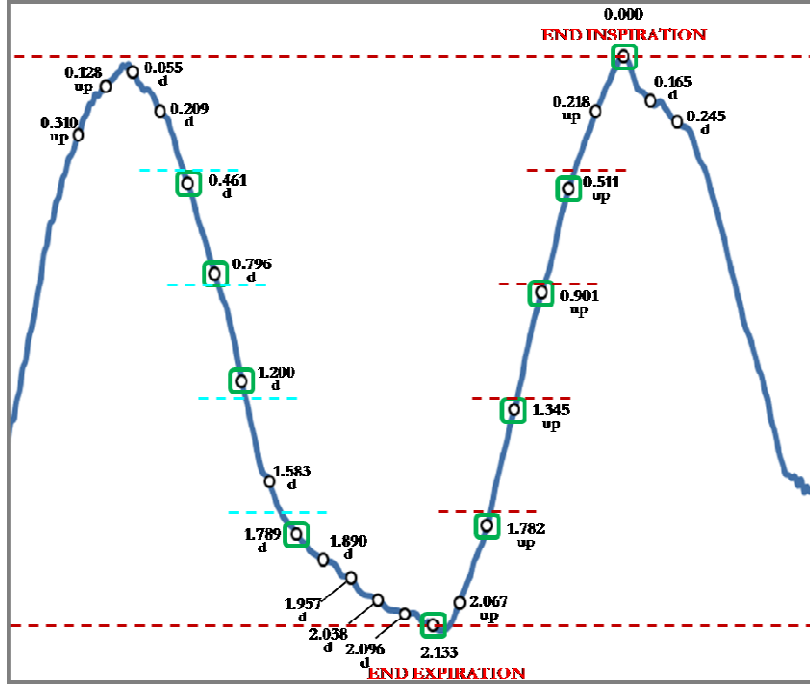


**Figure 13: Example of amplitude-binning applied to a single bed position.**

Sample patient data showing how the AB method selects images. On the respiratory waveform, white dots indicate an available cine CT image next to the associated amplitude and direction. The AB sorting identifies and selects the images associated with the min/max amplitude. Also, target amplitudes and direction are defined, and best-fit images are selected.

#### 3.2.2.4 4D-CT Sorting Mechanism Summary and Example

With the relative complexity of patient breathing, the application of PB, PC-PB, and AB sorting will lead to the selection of a different distribution of images. Figure 14 offers a clinical example of how, given the same input data, each 4D-CT sorting method will select different images to represent the different stages of breathing. In PB, we can see that the phase angle progression is linearly interpolated between the identified 0% points, and also that the 0% is not exactly at the maximum amplitude. In the PC-PB method, the 50% point is forced to the minimum amplitude, and that the phase values are dispersed evenly between 0% - 50% and between 50% and 0%. The shorter inspiration time leads to a more temporally condensed numerical phase from 50% to 0%. Finally, the



AB method forces the selection of the images at the extrema, and distributes the selection of other images along the vertical amplitude axis (identified as either inspiration or expiration).

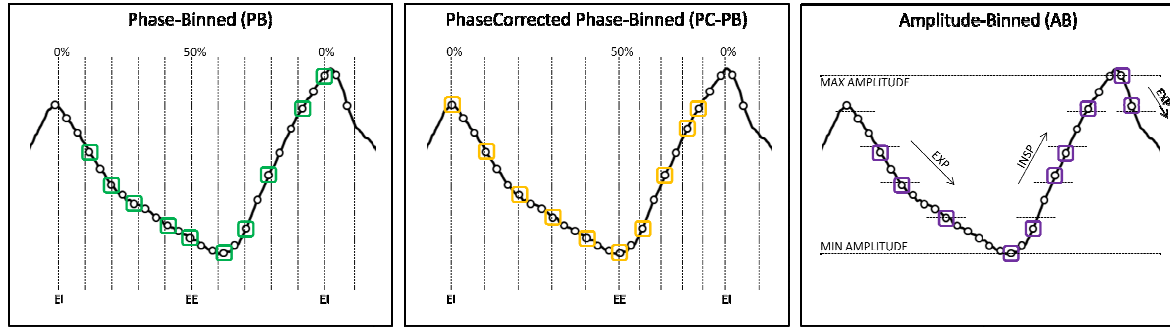


**Figure 14: 4D-CT summary selection process for PB, PC-PB, and AB.**

The selections of images for the three 4D-CT methods (PB, PC-PB, and AB). The difference in phase calculation can be seen between the PB (left) and PC-PB (middle). The AB method (right) forces the selection of the images at the extreme amplitudes.

### 3.2.3 RPM File Timing Calculations

We developed programs to quantitatively analyze the PC respiratory data file. We used the PC data file that defined the 50% point as the minimum amplitude to account for observed longer expiration times than inspiration time. Using a PC respiratory file also offered the opportunity to correct any incorrectly identified EI points in the original respiratory data file. The average breath cycle was defined as the time between subsequent EI points occurring within the duration of the cine scan. Similarly, we defined the average expiration time between the marked EI and EE, and the average inspiration time between the marked EE and EI points. We calculated the average ratio of expiration time to inspiration time to understand the level of breathing asymmetry when identifying the motion extrema as the EI and EE points.

We also calculated the estimated percentage of raw projection data not utilized when applying a 4D-CT sorting mechanism by comparing the average breath cycle and cine duration. Based on the data sufficiency condition (DSC) for a cine acquisition, we theoretically need projection data for the duration of only one breathing cycle plus one CT gantry rotation (17). We therefore defined the

percentage of unused raw data as 1 minus the ratio of the average DSC duration and the clinically utilized cine duration (i.e. beam-on time per bed position).

### **3.3 Results**

Twenty-eight patients (16 men and 12 women) who had previously undergone thoracic 4D-CT scans at our institution for the treatment of lung cancer were selected for this study. The average age was 76 years, ranging from 55 to 87 years. All of the tumors were classified as non-small cell lung cancer (NSCLC). Twenty-six of the patients were treated with stereotactic body radiation therapy (SBRT); two patients were treated with protons, but both had early stage NSCLC and were candidates for treatment with SBRT.

The clinical cine acquisition for our patients resulted in an average of 21.7 cine images available per slice location. The number of cine images available at each slice location was a function of patient-specific factors such as scan extent, cine duration and cine interval, as well as hardware limitations (maximum of 3000 reconstructed images per series).

Analysis of the PC respiratory file showed an average patient respiratory cycle of 4.2 s, a value comparable to prior studies using similar respiratory monitoring systems (32). The average time for expiration and inspiration was 2.7 s and 1.6 s, respectively, leading to an average ratio of expiration to inspiration time of 1.7. On average, an estimated 25% of the acquired CT data was unused when generating MIP from 4D-CT sorting methodologies.

## **4. SPECIFIC AIM 2: VOLUME MEASUREMENTS ON MIP DATA SETS**

### **4.1 Objectives**

In specific aim 2, we performed the volumetric measurements and comparisons among the four MIP data sets that we created. Images were sent to a commercial treatment planning system, and were automatically contoured using the available thresholding tools. From the volumetric results, we were able to proceed to compare and to analyze the quantitative differences that result in the appearance of the iGTV when generated from the different methods.

### **4.2 Methods and Materials**

The four MIP image sets for each patient were sent to a commercial radiation treatment planning system (Pinnacle 8.1w; Philips Healthcare, Madison, WI). To minimize the effect of human inter-observer variation, each data set was automatically contoured using a lower threshold of 600 (equivalent to -424 Hounsfield units) using the readily available tools within the software. The threshold value selected represented a value that maximized tumor volume, but limited volume growth into the surrounding lung parenchyma. The choice of tumors for this work made automatic contouring a reasonable estimate of the clinical (manual) contour, but also tended to emphasize smaller, less complex tumors with larger motions to amplify observed differences between the methods. The treatment planning software reported the total tumor volume, or iGTV in our case, based on the contoured tumors.

Since it is standard practice to add clinical margins to the visible tumor iGTV, we next added a uniform margin expansion of 5 mm to each patient's iGTV to arrive at a simulated planning target volume (PTV), as documented within Radiation Therapy Oncology Group (RTOG) 0915 for patients undergoing treatment with SBRT (1). The process of adding simulated margins was meant to give a baseline understanding of how differences that we observed in our iGTV measurements would be affected by applied expansions.

To compare the contoured volume measurements, we performed a paired t-test (two-sided alternative) between the  $MIP_{CINE}$  and each of the three  $MIP_{4D-CT}$  data sets. We also performed a two-tailed paired t-test between each of the  $MIP_{4D-CT}$  data sets.

#### **4.2.1      *Characterization of Tumor Size***

To characterize the size of each tumor, we measured the approximate static tumor volume and largest dimension on the clinically acquired 4D-CT 50% phase images, using an image workstation (Advantage Workstation 4.2; GE Healthcare, Waukesha, WI). The measurement was made on the 50% phase image because it was observed that most patients paused breathing near the end of expiration; this condition represented the best scenario to approximate a non-moving tumor. The image workstation has tools that allow the user to cut away the tissue surrounding the target volume. Then, we applied a CT number threshold (minimum of -406 Hounsfield units) to exclude low-density lung parenchyma. From the volume identified by the applied threshold, we measured and documented the static tumor volume. The tumor's largest dimension was measured on a standard three-plane view using a lung window.

#### **4.2.2      *Pinnacle Automatic Contouring***

All four of the MIP image sets were pushed to the TPS in order to automatically contour the tumor iGTV. The TPS has a collection of automatic contouring tools that we used to execute the contouring. Depending on the particular image slice, we primarily used one of two automatic contouring tools – the ‘autocontour tool’ and the ‘autocontour all tool.’ The autocontour tool places a single contour on a single slice. The user clicks to set the seed point, and the software finds the first structure within the specified density range and contours it. If the pixel value of the seed point lies *within* the threshold range, the contour is drawn on the pixels just before the value passes *out of* the range. If the pixel value of the seed point lies *outside* of the threshold range, the contour is drawn on the pixels just before the value crosses *into* the threshold range (33). Because of the slight difference

in contour placement for either case, the seed point was always placed within the tumor tissue. For cases that were more complicated, we defined a separate region of interest (ROI) and used the ‘autocontour all tool,’ which contours all structures on the slice within the threshold. Using this as a roadmap, we then manually traced the outline of the tumor. Figure 15 offers patient examples on which we used the automatic contouring tools. On the top, the ‘autocontour tool’ correctly identified the tumor without any other major intervention. On the bottom more complicated case, we used the ‘autocontour all tool’ to lay down a threshold roadmap around the tumor, and manually traced the tumor.

The selection of the threshold level was an important decision. We contoured the images with a lower threshold of 600 (equivalent to -424 HU). This threshold was selected based on suggestions by the Pinnacle manual, prior studies in the literature, and personal experience. The value represented a level that captured the tumor volume without expansion into the surrounding lung parenchyma.

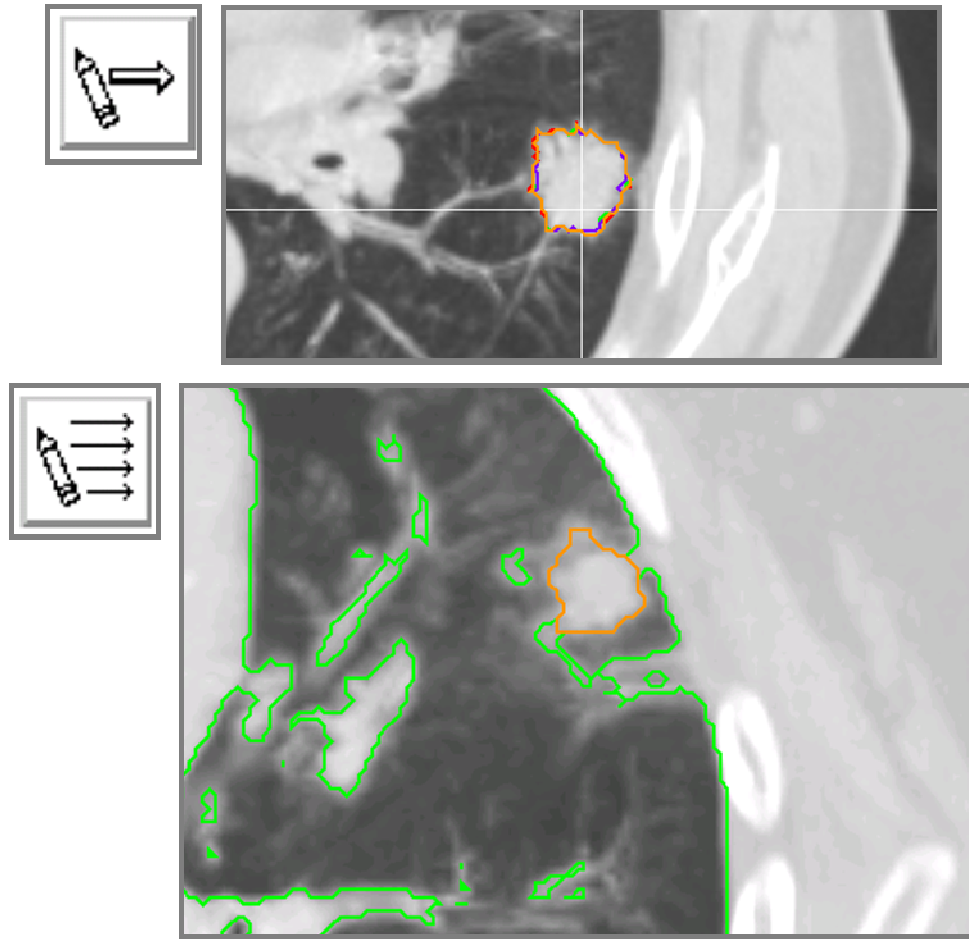


**Figure 15: Automatic contouring tools within treatment planning system.**

Top, the 'Autocontour tool' was used on very easily definable tumors. Bottom, for more complicated situations for which the 'Autocontour tool' was ineffective, we laid down a global threshold with the 'Autocontour all tool,' and manually traced the tumor.

### 4.2.3 Pinnacle Volume Calculations

After completing the iGTV contouring, we used the TPS to calculate the total contoured volume of the iGTV. The method used by the TPS to calculate is dependent on the location of the contour line. The pixels that lie within the contour are fully counted. A factor of 0.5 is applied to pixels that are intersected by a contour. A pixel that lies outside of the contour is not counted toward the volume at all. Figure 16 graphically shows how the pixel volumes are weighted by the TPS total contoured volume calculation.

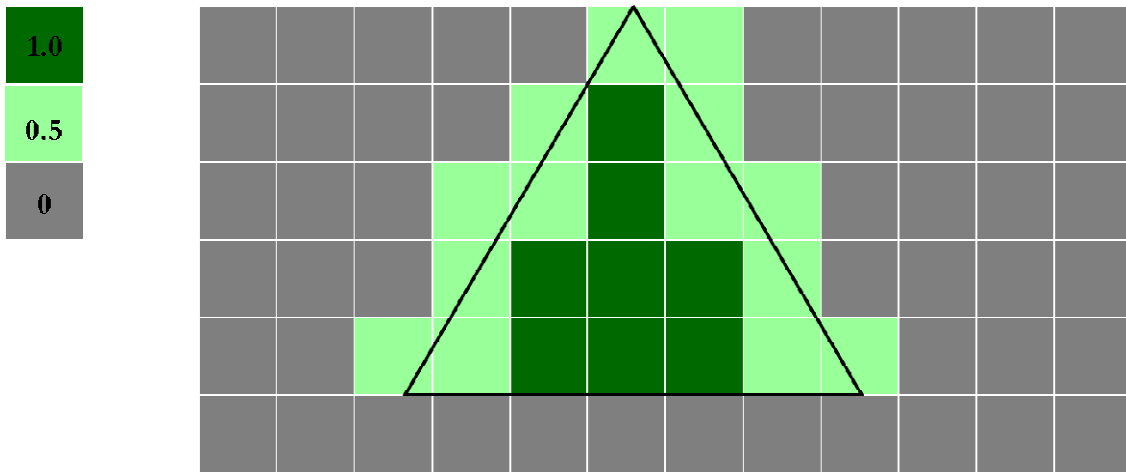


**Figure 16: Volume calculations using Pinnacle treatment planning system.**

For a given contour, shown as a black line, pixels that lie totally within have the entire pixel volume counted, pixels that intersect have half of the pixel volume counted, and pixels that are outside are not counted toward the total contoured volume.

The nominal pixel volume for our particular acquisition can be calculated based on the CT image matrix size, the image thickness, and the display field of view (DFOV). The standard matrix size for a CT image is 512 x 512. All of the patients were acquired with a DFOV of 50 cm and an image thickness of 2.5 mm. The calculation of the pixel volume is given by:

$$V_{\text{pixel}} = \left( \frac{\text{DFOV}}{\# \text{Pixels}} \right)^2 \times \text{Img Thk} = \left( \frac{500\text{mm}}{512\text{pixels}} \right)^2 \times 2.5\text{mm} = 2.4\text{mm}^3$$

In this study, the method of volume calculation used by the TPS was used to report the iGTV and PTV.

#### **4.2.4 Simulated Margin Expansion of iGTV**

The process of adding margins to the automatically contoured iGTV was possible with the tools in the TPS. The user can generate a new set of contours based on an input ROI plus or minus a desired margin. The applied margin can be a uniform expansion/contraction, or it can be modified by independently assigning a value to each direction (LR/AP/SI).

In our case, the source ROI was the iGTV that was automatically contoured for each of the four processing methods. We added a uniform 5 mm margin to the iGTV to arrive at the PTV. This simulated margin was selected based on RTOG 0915, which focuses on the delivery of SBRT (1), and is meant to account for setup uncertainty. Figure 17 shows an example of an automatically contoured iGTV as the source ROI as well as the

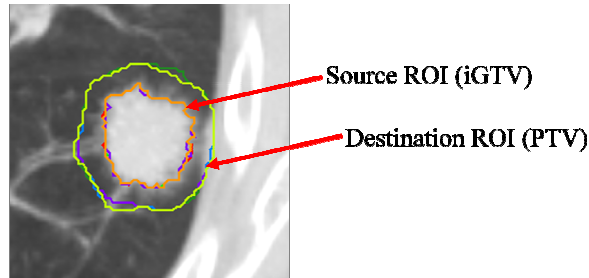


**Figure 17: Margin expansion applied to iGTV.**

Using the expansion/contraction tools, we applied a uniform expansion of 5 mm to the iGTV (source ROI) to arrive at the PTV (destination ROI).

### **4.3 Results**

The average total tumor motion was measured to be 1.5 cm, ranging from 1.0 cm to 2.9 cm. The average static tumor volume was 6.5 cm<sup>3</sup>, with an average largest dimension of 2.3 cm. Table 2 summarizes the results of the automatically contoured iGTV on each of the four MIP data sets. In all cases, the iGTV<sub>CINE</sub> had the largest magnitude. This makes theoretical sense, in that approximately twice as many images are used to build the MIP<sub>CINE</sub> as any of the MIP<sub>4D-CT</sub> image sets. Expressed as



a percentage of  $iGTV_{CINE}$ , our  $iGTV_{4D-CT}$  values ranged from 83.8% to 99.1%. Out of 84 4D-CT data sets (i.e. 28 patients with 3 4D-CT data sets per patient), 18 of the  $iGTV$  values were more than 10% smaller than the  $iGTV_{CINE}$ . For our patient population, 21.4% of the  $iGTV_{4D-CT}$  values were more than 10% smaller than the  $iGTV_{CINE}$ . Figure 18 shows the histogram associated with the results of calculating  $iGTV_{4D-CT}$  as a percentage of  $iGTV_{CINE}$ . The largest  $iGTV$  was captured by the PC-PB method for 20 of the patients, by the PB method for 5 of the patients, and by the AB method for 3 of the patients.

**Table 2: Summary of measured iGTV values.**

Summary of iGTV measurements for our cohort of 28 patients, using each of the four MIP data sets. Results are also presented in  $iGTV_{4D-CT}$  as a percentage of the larger  $iGTV_{CINE}$ .

Pt. No.	$iGTV_{CINE}$	$iGTV_{4D-CT,PB}$	$iGTV_{4D-CT,PC-PB}$	$iGTV_{4D-CT,AB}$	$iGTV_{4D-CT}$ as % of $iGTV_{CINE}$		
	(cm <sup>3</sup> )	(cm <sup>3</sup> )	(cm <sup>3</sup> )	(cm <sup>3</sup> )	PB	PC-PB	AB
1	10.9	10.3	10.4	10.3	94.7%	95.7%	94.3%
2	2.9	2.6	2.7	2.5	87.4%	90.7%	84.9%
3	5.6	5.4	5.5	5.3	96.6%	99.1%	95.7%
4	1.8	1.7	1.7	1.5	93.8%	95.3%	84.9%
5	10.7	9.5	10.0	9.4	88.4%	93.6%	88.0%
6	5.2	4.7	4.8	4.5	90.1%	91.4%	86.2%
7	11.8	11.1	11.4	11.0	94.0%	96.9%	93.7%
8	2.9	2.6	2.7	2.5	90.9%	92.3%	87.8%
9	16.8	15.8	16.1	15.4	94.1%	95.6%	91.4%
10	12.2	11.5	11.5	11.5	93.8%	94.3%	93.8%
11	4.3	4.1	4.0	4.0	95.0%	93.9%	93.8%
12	9.8	9.2	9.2	8.9	93.5%	93.8%	90.3%
13	7.3	7.0	7.1	7.1	95.1%	96.7%	97.7%
14	10.6	9.7	10.0	9.1	91.4%	94.2%	86.0%
15	3.5	3.1	3.1	2.9	88.2%	89.1%	84.7%
16	8.0	7.2	7.6	7.5	90.0%	94.3%	93.8%
17	6.9	6.4	6.5	6.2	93.0%	94.5%	90.7%
18	8.1	6.8	7.0	7.2	84.6%	86.2%	88.6%
19	0.9	0.9	0.9	0.9	96.9%	97.4%	95.3%
20	3.3	2.8	2.9	3.0	83.8%	89.4%	90.0%
21	11.1	10.4	9.9	10.2	93.1%	89.2%	92.1%
22	39.3	35.8	36.9	35.1	91.0%	93.8%	89.3%
23*	25.5	24.3	24.7	24.3	95.5%	96.8%	95.5%
24	4.8	4.6	4.5	4.6	95.7%	93.5%	95.0%
25*	53.7	53.0	52.7	52.1	98.7%	98.1%	97.0%
26	6.0	5.8	5.8	5.8	97.5%	97.5%	97.5%
27	19.8	19.4	19.5	18.8	97.8%	98.4%	94.8%
28	16.4	15.2	15.3	15.0	92.8%	93.5%	91.9%
Max	53.7	53.0	52.7	52.1	98.7%	99.1%	97.7%
Min	0.9	0.9	0.9	0.9	83.8%	86.2%	84.7%
Mean	11.4	10.7	10.9	10.6	92.8%	94.1%	91.6%
SD	11.6	11.2	11.3	11.0	3.8%	3.1%	4.0%

\*Patient was a candidate for SBRT, but was clinically treated with protons.

The results of the paired t-test (two-sided alternative) showed statistically significant differences between the  $iGTV_{CINE}$  and each of the three 4D-CT methods (all cases,  $p < 0.01$ ). Similarly, the two-tailed paired t-test indicated that there were statistically significant differences when comparing the 4D-CT methods to one another (all cases,  $p < 0.02$ ). Table 3 shows the p-values for each combination of iGTV measurement comparisons.

**Table 3: Paired t-test results comparing iGTV measurements.**

Paired t-tests (two-tailed) were performed between each of the four iGTV measurement methods. For all permutations, the p-value was below 0.05, indicating a statistically significant difference between each of the methods.

Method A	Method B	p-value
$iGTV_{CINE}$	$iGTV_{4D-CT,PB}$	$< 0.01$
$iGTV_{CINE}$	$iGTV_{4D-CT,PC-PB}$	$< 0.01$
$iGTV_{CINE}$	$iGTV_{4D-CT,AB}$	$< 0.01$
$iGTV_{4D-CT,PB}$	$iGTV_{4D-CT,PC-PB}$	$< 0.02$
$iGTV_{4D-CT,PB}$	$iGTV_{4D-CT,AB}$	$< 0.02$
$iGTV_{4D-CT,PC-PB}$	$iGTV_{4D-CT,AB}$	$< 0.01$

The differences that we observed between the  $iGTV_{CINE}$  and the  $iGTV_{4D-CT}$  measurements diminished after adding the simulated uniform margin expansions. The smallest  $PTV_{4D-CT}$  as a percentage of  $PTV_{CINE}$  that we observed was 87.6%, as shown in Table 5. Though the  $PTV_{4D-CT}$  as a percent of  $PTV_{CINE}$  appeared to approach unity as we added expansions, it is important to note that the volume of affected tissue is larger per percentage point for the PTV than for the iGTV (i.e., 1% of the PTV is larger in magnitude than 1% of the iGTV). Figure 18 shows the histogram of results related to the  $PTV_{4D-CT}$  as a percentage of  $PTV_{CINE}$ . In the figure, we can observe that adding the 5 mm margin to the iGTV caused the 4D-CT target volume as a percentage of cine target volume to shift toward unity. A comparison of PTV values with a two-tailed paired t-test showed statistically significant differences between each set of measurements, as shown in Table 4 below.

**Table 4: Paired t-test results comparing PTV measurements.**

Paired t-tests (two-tailed) were performed between each of the four PTV measurement methods. For all permutations, the p-value was below 0.01, indicating a statistically significant difference between each of the methods.

<b>Method A</b>	<b>Method B</b>	<b>p-value</b>
PTV <sub>CINE</sub>	PTV <sub>4D-CT,PB</sub>	< 0.01
PTV <sub>CINE</sub>	PTV <sub>4D-CT,PC-PB</sub>	< 0.01
PTV <sub>CINE</sub>	PTV <sub>4D-CT,AB</sub>	< 0.01
PTV <sub>4D-CT,PB</sub>	PTV <sub>4D-CT,PC-PB</sub>	< 0.01
PTV <sub>4D-CT,PB</sub>	PTV <sub>4D-CT,AB</sub>	< 0.01
PTV <sub>4D-CT,PC-PB</sub>	PTV <sub>4D-CT,AB</sub>	< 0.01

**Table 5: Summary of measured PTV values.**

Summary of PTV measurements for our cohort of 28 patients, using each of the four MIP data sets. Results are also presented in  $PTV_{4D-CT}$  as a percentage of the larger  $PTV_{CINE}$ .

Pt. No.	$PTV_{CINE}$	$PTV_{4D-CT,PB}$	$PTV_{4D-CT,PC-PB}$	$PTV_{4D-CT,AB}$	$PTV_{4D-CT}$ as % of $PTV_{CINE}$		
	(cm <sup>3</sup> )	(cm <sup>3</sup> )	(cm <sup>3</sup> )	(cm <sup>3</sup> )	PB	PC-PB	AB
1	35.2	33.5	34.2	33.2	95.3%	97.3%	94.2%
2	16.4	15.4	14.7	14.4	94.0%	89.9%	87.8%
3	20.7	20.2	20.6	20.2	97.6%	99.6%	97.6%
4	10.7	10.4	10.5	9.8	97.1%	98.2%	91.5%
5	34.2	31.9	33.4	31.5	93.3%	97.6%	91.9%
6	22.0	20.5	20.7	19.3	93.1%	94.1%	87.6%
7	35.7	34.1	35.1	34.0	95.5%	98.5%	95.4%
8	16.2	15.3	15.5	15.1	94.6%	96.1%	93.4%
9	46.4	44.5	44.5	43.4	95.9%	95.9%	93.5%
10	43.4	42.2	42.0	41.8	97.2%	96.7%	96.3%
11	18.1	17.3	17.5	17.5	96.0%	97.2%	96.9%
12	34.2	32.3	32.7	31.2	94.6%	95.6%	91.4%
13	25.4	24.6	24.8	25.1	96.7%	97.7%	98.7%
14	33.0	31.0	31.8	30.0	93.8%	96.4%	90.8%
15	17.5	16.4	16.9	16.1	93.7%	96.5%	92.1%
16	26.7	24.7	25.8	25.5	92.5%	96.6%	95.6%
17	24.9	23.7	24.1	23.5	95.5%	96.9%	94.4%
18	27.7	25.5	25.8	26.0	92.3%	93.1%	93.8%
19	7.1	7.0	7.0	7.0	97.9%	98.5%	97.8%
20	18.9	17.9	18.2	17.8	94.7%	96.4%	94.3%
21	39.3	37.5	38.3	36.8	95.4%	97.6%	93.8%
22	90.3	84.1	86.7	82.9	93.2%	96.0%	91.8%
23*	73.7	71.6	72.1	71.7	97.1%	97.8%	97.2%
24	20.2	19.7	19.5	19.2	97.5%	96.6%	95.0%
25*	133.1	131.9	131.1	131.8	99.1%	98.5%	99.0%
26	21.8	21.4	21.3	21.4	98.4%	98.1%	98.6%
27	53.6	52.5	52.8	51.6	98.0%	98.7%	96.3%
28	44.8	42.4	42.6	42.1	94.8%	95.1%	94.1%
Max	133.1	131.9	131.1	131.8	99.1%	99.6%	99.0%
Min	7.1	7.0	7.0	7.0	92.3%	89.9%	87.6%
Mean	35.4	33.9	34.3	33.6	95.5%	96.7%	94.3%
SD	26.4	25.8	25.9	25.8	1.9%	1.9%	3.0%

\*Patient was a candidate for SBRT, but was clinically treated with protons.

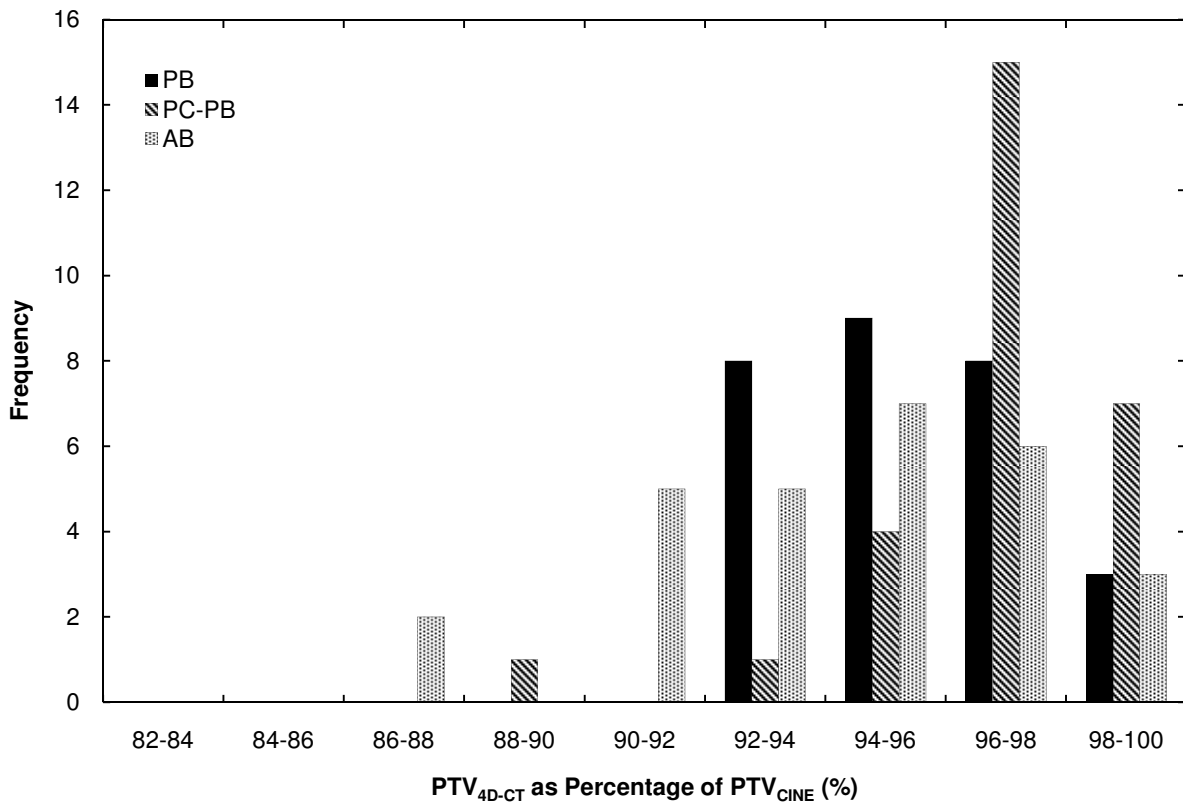
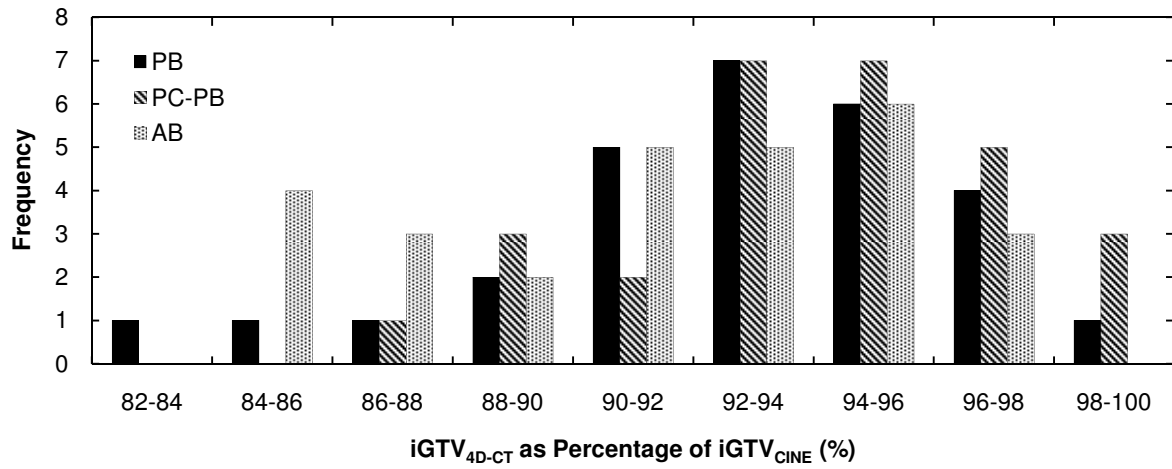


**Figure 18: Histogram of target volume results.**

Top, histogram of  $iGTV_{4D-CT}$  as a Percentage of  $iGTV_{CINE}$ . Bottom, histogram of  $PTV_{4D-CT}$  as a percentage of  $PTV_{CINE}$ . Histograms show that addition of margins cause the 4D-CT target volume as a percentage of cine target volume to shift toward unity.

## **5. SPECIFIC AIM 3: INVESTIGATION OF CAUSES OF IGTV DIFFERENCES**

### **5.1 Objectives**

Specific aim 2 quantified the volume differences that were measured on the four MIP image sets that were created previously. In specific aim 3, we created a method to understand some of the mechanisms that lead to the observed volume differences.

### **5.2 Methods and Materials**

We created a method of compiling important information together with the aim of understanding why we observed target volume differences measured between each of the four MIP data sets. In 4D-CT, multiple sources of data are used, including the respiratory data file and the cine CT images. Also, with each 4D-CT sorting method, we have a collection of images that are selected based on their associated phase or amplitude. Understanding the relationship between the final MIP and the constituent images required a means by which to track what images were selected and what portions of the iGTV were being affected by those selections. To do so, we developed programs to pull pertinent information from the images (cine CT and 4D-CT images) and from the respiratory data file. The information from both was compiled into a spreadsheet that allowed us to simultaneously reference the numerical and graphical data.

#### ***5.2.1 Composite Overlay of Respiratory Trace and Selected 4D-CT Images***

To understand how the distribution of selected images affects the generated MIP and resultant iGTV, we correlated the measured respiratory waveform and the selected images for each of the three 4D-CT methods. Combining information from the different data sources required the implementation of a collection of tasks:

- 1) Pulling information from the respiratory data file
  - a. Identified EI and EE points

- b. X-ray beam status (beam-on or beam-off)
- 2) Pulling information from the CT images
  - a. Image series (for identification of image bin)
  - b. Image number
  - c. Image slice location
  - d. Image mid-scan time
- 3) Associating amplitude to each CT image
- 4) Aligning time scale of data file with image mid-scan times
  - a. Initial beam-on time for each bed position
  - b. Image mid-scan time of first cine image generated at each bed position
- 5) Compiling all data into a single spreadsheet.

We developed programs to extract header information from the CT images (cine and 4D-CT) including the image mid-scan time, slice location, image bin, and image number. We also developed programs to analyze and extract data from the respiratory data file. For the purpose of creating the composite overlay, we extracted the EI and EE points and the time of the first beam-on indicator for each bed position. Sections 5.2.1.1 and 5.2.1.2 describe the other processes that were used to create the composite overlay.

#### *5.2.1.1 Temporal Alignment of RPM Data and Image Mid-scan Times*

The time stamps in the respiratory data file and the cine CT image times are not base-lined to the same time scale. To create the composite overlay of the respiratory trace and selected 4D-CT images, a time alignment was required. As previously discussed, the RPM file contains amplitude measurements of the reflective block placed on the patient's torso at a frequency of 30 Hz (one sample every ~33 msec), and the state of the x-ray beam (beam on or beam off) tracked at the same frequency. Similarly, images that are created by the CT scanner are tagged with an image mid-scan time, available within the DICOM image header (0019, 1024). The image mid-scan time is the time



at which half of the data is collected for a full 360° acquisition. In our study, the amount of time required to generate an image is equal to a full tube rotation time, or 0.5 s; the image mid-scan time would be 0.25 s. Figure 19 graphically depicts the relation between the mid-scan time stamp and the temporal window of the image.

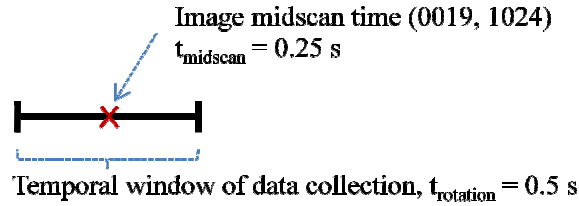


**Figure 19: Relationship between mid-scan time and image temporal window.**

The relationship between the mid-scan time stamp and the temporal window of the image data collection is represented by the graphic. The black ‘I-beam’ shape represents the data collection window, and is equal to the gantry rotation time. Each image has a DICOM stamp (0019, 1024) with the image mid-scan time, which is marked at the center of the data collection time.

Upon first examination, it appeared as though the RPM time scale and the mid-scan times of the generated CT images are unassociated; therefore, temporal matching the images with the respiratory data file was necessary. To correlate the two time scales, a correction factor can be applied to the image mid-scan times. The correction factor is meant to shift the start of CT image data collection to the initial beam-on indicator from the RPM file. In practice, the mid-scan time of the first image created is shifted to occur half of a rotation time after the RPM beam-on indicator. After calculating a correction factor and applying it to all images, we found that the images at the first bed position were properly aligned; however, subsequent bed positions lost the alignment. Figure 20 shows a schematic depicting the proper alignment of the cine CT images at the first bed position to the RPM beam-on indicator as well as the misalignment of the cine CT images created at the second bed position.

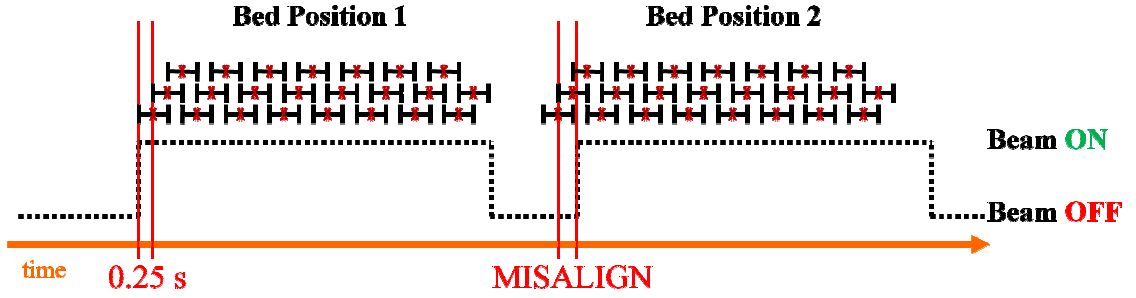


**Figure 20: Graphical representation of RPM and image time alignment.**

After applying a correction factor to align the images at the first bed position, the subsequent bed positions continued to be mis-aligned.

To explore the cause of the loss of temporal alignment in subsequent bed positions, we compared the x-ray beam-on and beam-off times as calculated from the RPM file and as calculated from the cine CT image mid-scan times. Calculation of the beam-on and beam-off times from the RPM file was trivial, and only required the development of software to reference the available beam status indicators and time stamps within. The calculation of beam-on and beam-off times from the images required more effort. Figure 21 schematically shows the process of the beam timing calculations from batches of cine images created at different bed positions. It shows that the beam-on time can be calculated by measuring the absolute difference in mid-scan times between the first and last image created at one bed position, plus one CT gantry rotation time. The addition of one CT gantry rotation time accounts for the fact that there is half a tube rotation before the first mid-scan time marker and half a tube rotation time after the last mid-scan time marker. Similarly, the beam-off time can be calculated as the absolute difference between the mid-scan time of the last image created at one bed position and the first image created at the next bed position, minus one tube rotation time. The subtraction of one tube rotation time again accounts for data collection adjacent to the mid-scan time stamps. To perform the calculations, we developed software to pull header information from the cine CT images and to calculate the beam timing characteristics.

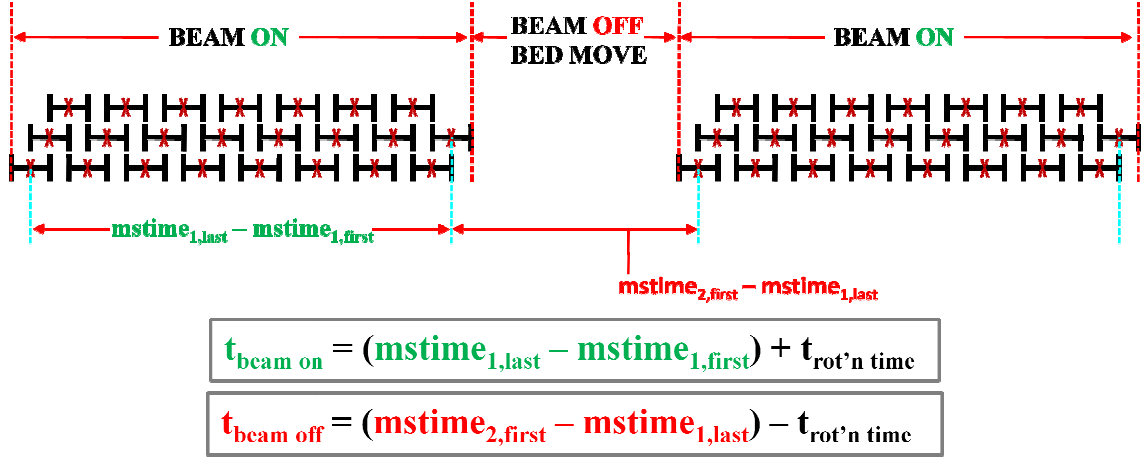


**Figure 21: Schematic exhibiting beam on/off calculations from cine images.**

At each bed position, a collection of images is generated with a cine CT acquisition. Based on the image mid-scan times of those images, it is possible to calculate how long the x-ray beam is on and off, as shown by the presented equations.

The results of these beam timing calculations showed that there is an error in the marking of the image mid-scan tags between batches of cine CT images created at different bed positions. Table 6 offers an example of beam timing calculations for a patient scan consisting of seven bed positions.

**Table 6: Sample beam on/off calculations from RPM and cine CT images.**

Sample calculations of the time the beam is on or off (using the respiratory data file and the image times) showed an error in the mid-scan time tags between bed positions.

Bed Position	BEAM ON [msec]		BEAM OFF [msec]	
	RPM File	Image Midscan Time	RPM File	Image Midscan Time
1	8241	8250	1402	750
2	8275	8250	1367	1750
3	8242	8250	1402	750
4	8274	8250	1335	1750
5	8274	8250	1368	1750
6	8275	8250	1368	750
7	8275	8250	n/a	n/a

The beam-on times remained consistent for all bed positions. We observed some small variance of beam-on times measured by the RPM system; this slight variance is caused by the discrete nature

of the RPM sampling of the beam status. The same slight variance was observed in the RPM beam-off timing calculations, and was also a result of the discrete sampling. We were surprised to find that the beam-off times calculated from the cine CT images showed inconsistency between each bed position. The sample provided in Table 6 shows that the x-ray beam was off between bed positions for either 0.75 s or 1.75 s. The calculated image beam-off time exhibited this inconsistency and sporadic switching between two values for the entire collection of patients in our study. Since we did not observe the same level of variance in the calculation of beam-off time using the respiratory data file, we believe this to be one of the primary causes of the significant temporal mismatch between the RPM and image time scales in subsequent bed positions. Because of this error in the image mid-scan time tag, one must apply the correction factor to each collection of cine CT images *at each bed position*. For the initial x-ray beam-on indicator at bed position  $n$  ( $T_{\text{beam-on}}$ ), a mid-scan time of the first produced image at bed position  $n$  ( $T_{\text{mid-scan}}$ ), and a known gantry rotation time ( $T_{\text{rotn}}$ ), the correction factor is:

$$CF_n = T_{\text{beam-on}} - T_{\text{mid-scan}} + 0.5 * T_{\text{rotn}}$$

The addition of the correction factor forces the start of CT data collection (one-half tube rotation before the mid-scan time of the first image) to the detected beam-on status indicator in the respiratory file. Table 7 shows sample calculations of the correction factor to be applied to the collection of generated images at each bed position. In each case, the corrected image mid-scan time occurs half of a gantry rotation (250 msec) after the initial beam-on indicator in the respiratory data file.

**Table 7: Sample calculation of image mid-scan time correction factors.**

An example showing the calculation of image mid-scan time correction factors, using the given equation. For each bed position, the correction factor is calculated from the beam-on time in the respiratory data file ( $T_{\text{beam-on}}$ ), the mid-scan time of the first image created at that bed position ( $T_{\text{mid-scan}}$ ), and the gantry rotation time ( $T_{\text{rotn}}$ ). Note that the corrected  $T_{\text{mid-scan}}$  is 250 msec (half gantry rotation) after the  $T_{\text{beam-on}}$ .

Bed Position	$T_{\text{beam-on}}$ [msec]	$T_{\text{mid-scan}}$ [msec]	$T_{\text{rotn}}$ [msec]	Correction Factor	Corrected $T_{\text{mid-scan}}$ [msec]
1	42750	975250	500	-932250	43000
2	52393	984250	500	-931607	52643
3	62035	994250	500	-931965	62285
4	71679	1003250	500	-931321	71929
5	81288	1013250	500	-931712	81538
6	90930	1023250	500	-932070	91180
7	100573	1032250	500	-931427	100823

#### 5.2.1.2 *Compiling Respiratory and Image Data*

Finally, the information what we pulled from the respiratory data file and from the CT images, along with the process we developed to align the two time scales were compiled into a single spreadsheet. The image data that was pulled from each of the three 4D-CT image sets and from the cine CT data set were imported. Also, the respiratory data file was imported. The correction factors used to align the image times with the respiratory data file were calculated and applied to all of the image mid-scan times. Each image was associated with an amplitude from the respiratory data file by using a Microsoft Excel macro that we developed.

Then we took the corrected data and started graphing it. We overlaid the respiratory waveform with indicators showing the cine CT images that were generated during the scan. We also created indicators to show what images were selected for each of the 4D-CT sorting methods. By using the graph and the parsed data, we were able to trace back what image was being selected for each method, and how it related to the final measured iGTV.

### 5.3 Results

The final output from the compiled data consisted of list data from the respiratory file and the images as well as a graph. We created this data for the entire collection of patients. Figure 22 shows an example of the composite overlay graph. The respiratory waveform has the temporally corrected cine CT images and the three 4D-CT image selections indicated. As well, the beam status and the identified EI and EE points are identified. Using the list data and collection of images, we were able to identify what bed positions captured the tumor motion envelope. Also, we could identify what images were selected and could correlate those selections to the MIP data sets that we generated.

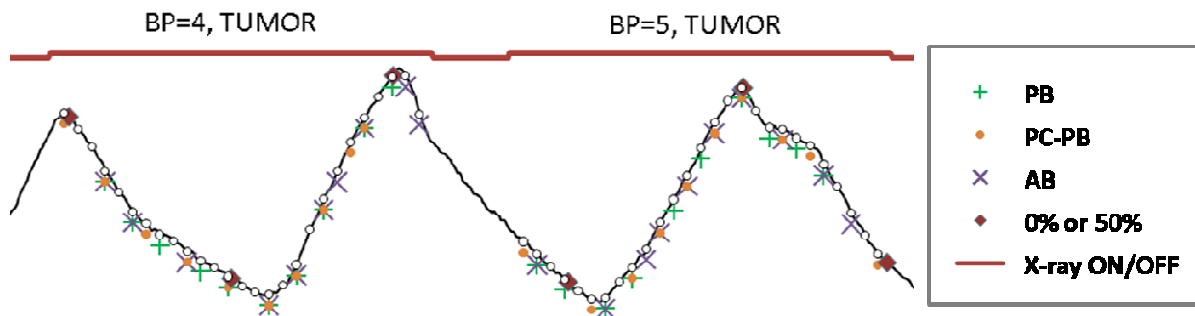


**Figure 22: Example of respiratory waveform and image composite overlay.**

Clinical example of composite overlay of respiratory waveform and CT images. The respiratory waveform shows the available cine CT images (white dots) and the identified 0% or 50% points. Images selected by each of the three 4D-CT sorting methods are indicated with their own symbol. The symbols indicating 4D-CT selection are translated directly downward from the waveform for ease of visualization.

#### 5.3.1 Duplicate Image Selection

By analyzing the composite overlay, it became apparent that situations existed in which an identical image was selected as the best fit for two adjacent bins. In other words, for a given bed position, less than 10 unique images were being selected. This has important implications when developing a MIP from the 4D-CT images, as our data indicates that using fewer images to build the

MIP will cause volume contraction from the larger  $iGTV_{CINE}$ . Figure 23 offers a clinical example for which both a PC-PB and an AB sorting methodology led to the selection of an identical image for two adjacent bins.

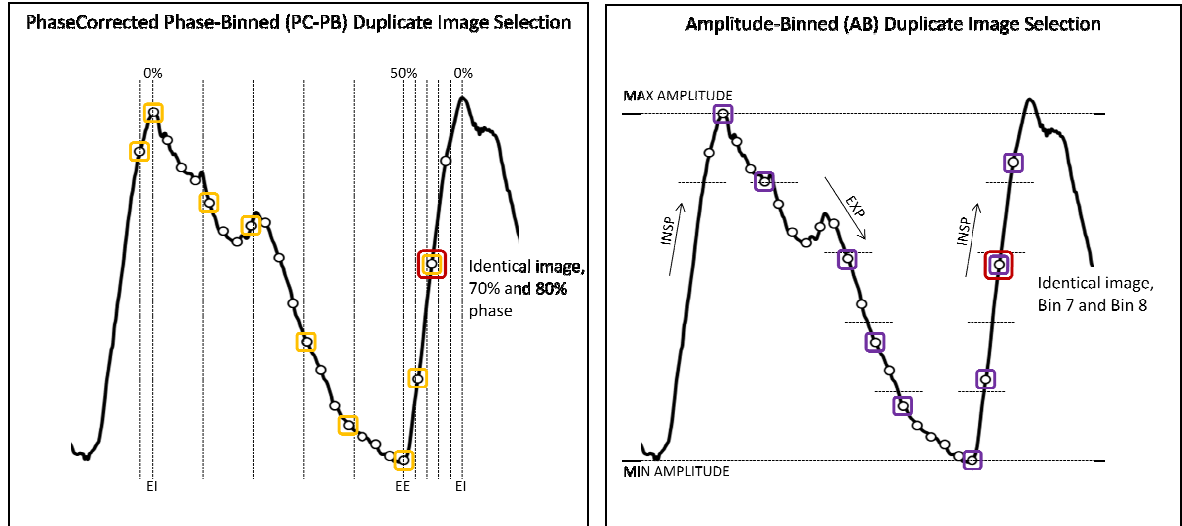


**Figure 23: Cause of duplicate image selection in PC-PB and AB.**

Clinical example of a breathing cycle and its associated cine CT image mid-scan times. White circles on the waveform indicate an available cine CT image from a single bed position. A single box indicates that cine CT image was selected by the PC-PB method (left) or the AB method (right). A double box indicates that a particular cine CT image was selected for two adjacent bins. A particularly short inhalation period or steep amplitude measurement (high time rate of change of amplitude) led to a higher likelihood of duplicate image selection with PC-PB and AB sorting.

Figure 24 illustrates the distribution of adjacent bin pairs that exhibited duplicate image selection for each of the 4D-CT image sorting processes over the entire scan extent. Image duplication occurred most frequently in the AB data set (which affected 25 of the patients), followed by PC-PB sorting (17 affected patients), and PB sorting (4 affected patients). When considering only the bed positions that captured the tumor, image duplication affected 18 patients with the AB method, 6 patients with the PC-PB method, and 2 patients with the PB method. The PB method generally

showed a uniformly distributed low frequency of image duplication occurrences, and duplication tended to be associated with irregular fast breathing. When PC-PB sorting was used, duplication tended to occur during the inspiration phase (between 50% and 100%) of the breath cycle. This phenomenon can be explained by our results from the analysis of the PC respiratory waveform data showing that the inspiration portion of the waveform (50%-100%) was temporally shorter than the expiration portion. In effect, the sorting process attempted to select more images than were available in the shorter inspiration time. The AB method exhibited two distinct regions of image duplication occurrences. The steep portions of the respiratory waveform were associated with a high time rate of change of amplitude. The sorting process attempted to select more images than were available in a short period of time during the steep portions of the inspiration and expiration. Figure 25 graphically shows the regions of high phase-rate and amplitude-rate regions of the respiratory waveform. Those regions correspond to the regions of image duplication shown in Figure 24.

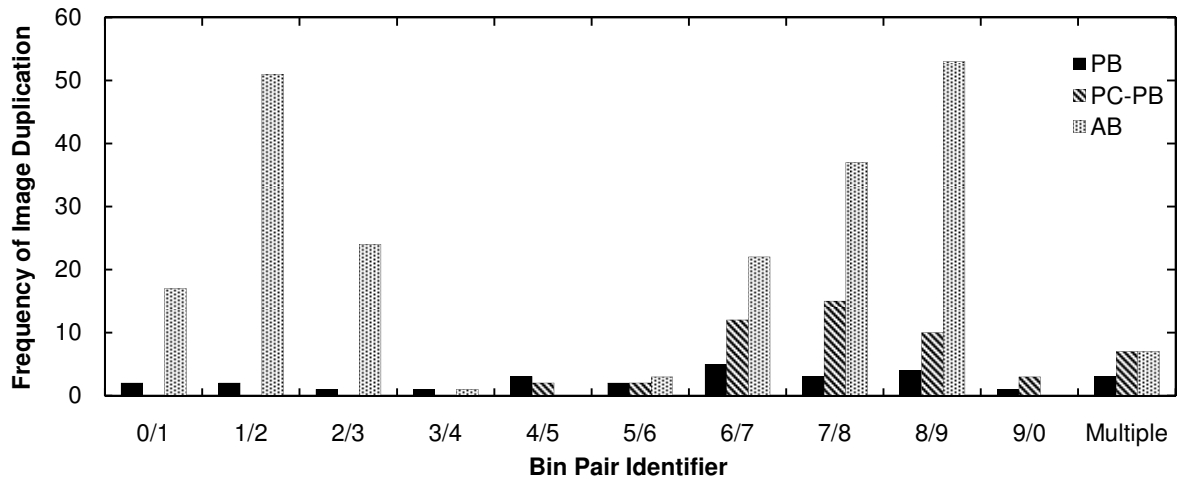


**Figure 24: Distribution of duplicate image selection by adjacent bin pair.**

Distribution of adjacent bin pairs that included duplicate images for each of the three 4D-CT sorting processes. This distribution was used to identify what portion of the breathing cycle was most susceptible to duplicate image selection for each method.



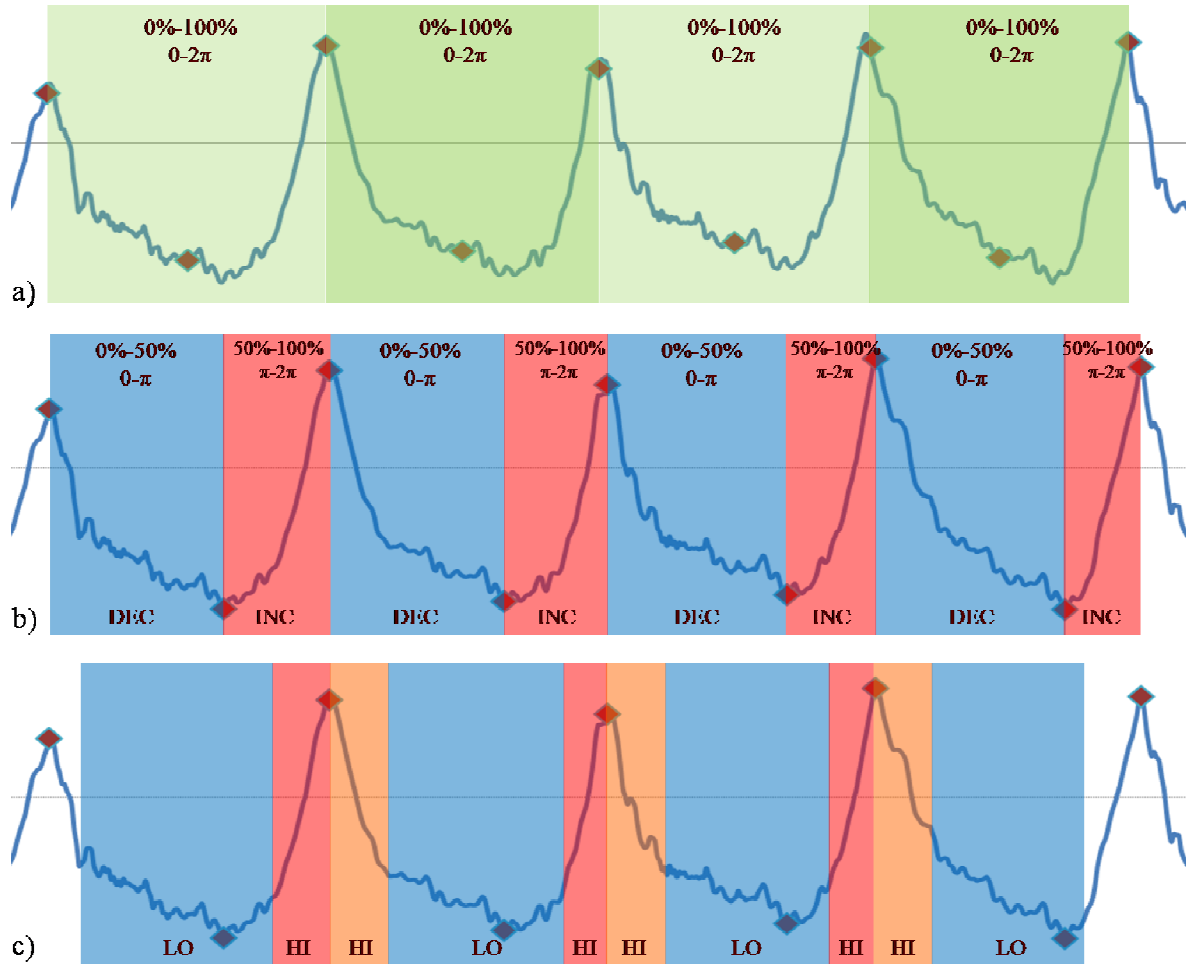


**Figure 25: Regions of high phase- and amplitude-rate on respiratory waveform.**

Respiratory waveform with 0% and 50% points identified for each 4D-CT sorting method, indicated by a diamond. (a) Phase calculations in PB are linearly interpolated between identified 0% points, with a constant phase-rate (time rate of change of phase) within. (b) Phase calculations in PC-PB are linearly interpolated between 0% - 50% and 50% - 100%. With an asymmetric breathing cycle (shorter time for inspiration than expiration), two different regions of phase-rate are formed – in comparison to the PB, the expiration phase has a decreased phase-rate, and the inspiration phase has an increased phase-rate. (c) The amplitude-rate (time rate of change of amplitude) is high during the steep upward portion of inspiration and the steep downward portion of the expiration.

### 5.3.2 *Error in Selection of Maximum Extent Image*

During the automatic contouring process, we observed cases for which the superior portion of the  $iGTV_{CINE}$  indicated the presence of lung tumor that the  $iGTV_{4D-CT}$  did not capture. To investigate, we used our data that correlated the respiratory waveform and the selected 4D-CT images. We found that the image associated with the minimum amplitude measurement did not always correlate to the image that showed maximum tumor motion extent on the superior portion of the contoured  $iGTV$ .

Figure 26 provides a clinical example of a series of cine CT images generated during a 4D-CT scan. Images that were selected by an AB methodology are identified. Images a) through d) represent a chronological series of images near the EE point, all located in the same slice location at the superior portion of the tumor motion envelope. As we progress forward in time from image a) to image d), we see the tumor become more visible and then start to diminish again. Since image d) was associated with the lowest amplitude, it was selected by the AB sorting methodology, even though the appearance of the tumor was diminished. Furthermore, since the images immediately before image d) that do show full motion extent have similar amplitudes, they were not selected; the nearest selected prior image was reconstructed a full 1.5 s before image d), and showed no tumor tissue. The contoured  $MIP_{CINE}$  and  $MIP_{4D-CT,AB}$  at that bottom of Figure 26 exhibit the missing tumor tissue not visible in the AB image selection.

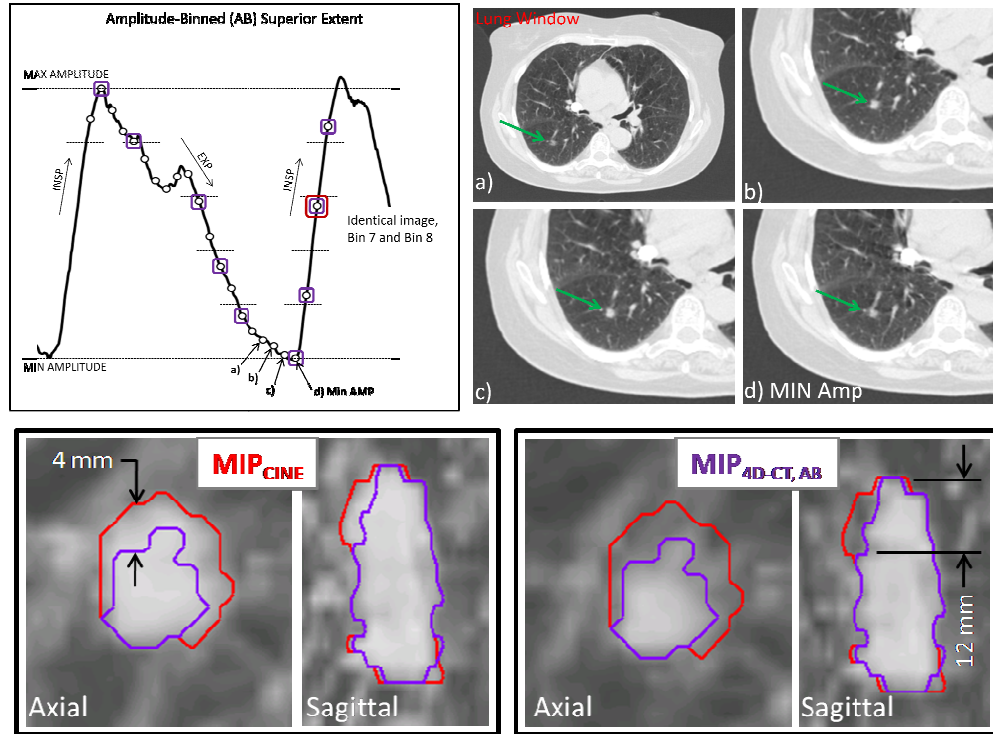


**Figure 26: Clinical example of error in selection of maximum extent image.**

Top, clinical example of (left) a breathing cycle with boxed AB selections and (right) of the mismatch between the image at minimum amplitude (d) and visualization of maximum tumor motion (b or c). Image (a) shows the tumor starting to move into the image plane as the patient exhales. Image (c), occurring 0.3 s prior to the minimum RPM amplitude image, has the highest tumor visibility and density. Image (d), associated with the extreme amplitude measurement exhibits suppressed density and blurred visualization. Bottom, contouring shows (right) that  $MIP_{4D-CT, AB}$  does not exhibit full visualization of the superior portion of tumor motion envelope when compared to (left)  $MIP_{CINE}$ . All of the axial images were taken from superior portion of tumor motion envelope.

## 6. DISCUSSION

Based on the results of this study, we developed a collection of clinical recommendations related to the usage of MIP in the delineation of target volumes. As well, we identified possible avenues for future work in the field of 4D-CT and target delineation.

### 6.1 Clinical Recommendations

This study quantified the differences in the iGTV when generating the MIP from three 4D-CT sorting methods and from the entire cine CT data set for tumors exhibiting motion of at least 1 cm. While in most cases the  $iGTV_{4D-CT}$  generated from the 4D-CT MIP closely approximated the  $iGTV_{CINE}$  generated from all the cine CT images, we did identify some situations for which the motion extent was under-represented in the  $MIP_{4D-CT}$  by more than 10%. Since a  $MIP_{4D-CT}$  is built from a subset of the available cine CT images (only 10 binned images as opposed to the 20-40 images available from cine CT), we mathematically expect that it will be smaller than  $MIP_{CINE}$ , becoming more apparent in patients having higher amplitude tumor motions.

Of particular interest in this study were the clinical cases in which the  $iGTV_{4D-CT}$  was significantly smaller than the  $iGTV_{CINE}$ . This study and others have identified reasons that the captured target volume with 4D-CT is smaller (34). It has been shown that PB methodologies do not explicitly select the images corresponding to the extreme amplitudes (35). When multiple EE or EI points are identified at a single bed position, only the best-fit phase image is selected without regard to maximum amplitude. The development of AB was meant to alleviate this issue. However, this study has shown that the image from an extreme-amplitude measurement does not always represent the maximum tumor motion extent; therefore, one cannot assume that selection of the extreme-amplitude images will capture the largest representative tumor volume from a given acquisition. This mismatch may occur for a variety of reasons, such as phase lag between the respiratory trace and the internal anatomy. Also, the image that is created at the minimum amplitude has a temporal window equal to the rotation time (36) (0.5 s in our clinic). Figure 27 shows the temporal window of an

image overlaid onto a respiratory waveform, using the clinical example presented in Figure 26. In the example, the patient inhaled sharply after the minimum amplitude was reached, indicating that the tumor likely moved out of the imaging plane while the image data were being collected, resulting in a blurred lower-density tumor appearance.

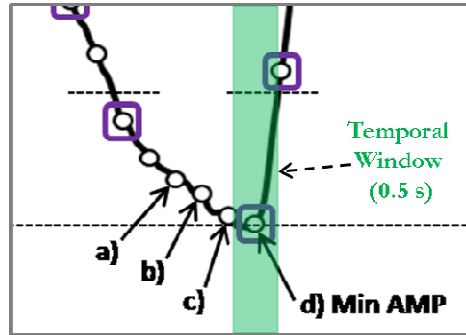


**Figure 27: Temporal window of CT image.**

Left, temporal window of the image at minimum amplitude overlaid on the respiratory waveform for the clinical case presented in Figure 26. The temporal window captures a large portion of the inhalation phase, causing the blurry appearance of image d).

It should be noted that the selection of an incorrect maximum extent image can also exist with a PB methodology. In particular, in PC-PB we identify the EE or 50% phase as the minimum amplitude and the EI or 0% phase as the maximum amplitude. This definition leads to a strong likelihood that the image closest to the minimum amplitude will be selected as the 50% phase image. However, the PC-PB method may still capture the image of maximum motion extent. Whereas the AB method ignored the neighboring prior images because they had similar associated amplitudes, the PC-PB method distributes the selected images approximately evenly across the time axis from 0% to 50% and may inadvertently select a more appropriate maximum extent image in a different image bin. The  $MIP_{4D-CT,PB}$  and the  $MIP_{4D-CT,PC-PB}$  (see Figure 28) closely approximated the tumor appearance in the  $MIP_{CINE}$ , whereas the  $MIP_{4D-CT,AB}$  did not.

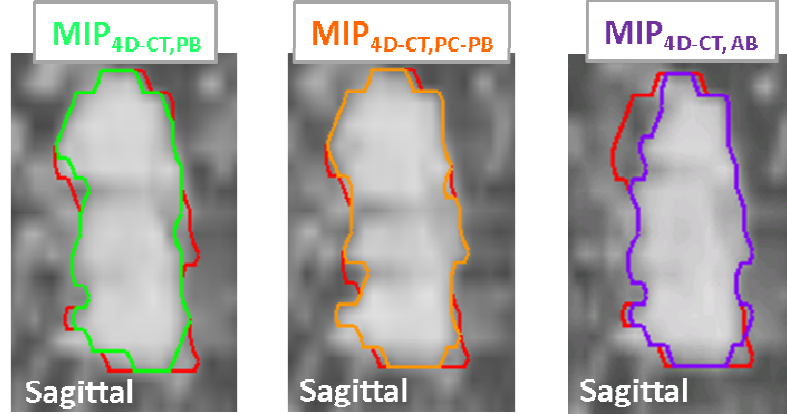


**Figure 28: MIP images for PB and PC-PB clinical example.**

For the clinical case presented in Figure 26, the PB and PC-PB methodologies selected a correct image at the superior edge of the iGTV. The AB selected the minimum amplitude image, but it did not correspond to the maximum extent.

This study has also shown that retrospective 4D-CT sorting is susceptible to the selection of the same image for multiple bins. From the perspective of the MIP, fewer constitutive images will lead to a smaller resultant iGTV, and should theoretically be more apparent for highly mobile tumors. *Because of the potential for misses when generating a MIP from a 4D-CT image set, we believe that there is merit in using the  $MIP_{CINE}$  to evaluate tumor motion extent.* By using the  $MIP_{CINE}$ , one can reliably expect that the visual representation of the iGTV will include all tumor positions captured by the CT acquisition. The tradeoff for a more representative iGTV with  $MIP_{CINE}$  is that the image set does exhibit higher anatomical noise – surrounding lung parenchyma appears denser and there is a slight loss of contrast between the tumor and surrounding tissue. However, this loss of contrast did not adversely affect our automatic contouring process.

It has been previously suggested that one could bypass the 4D-CT sorting process, instead relying on the MIP and RACT generated from the entire cine CT data set (20, 35). By doing so, one could minimize or even avoid the extra expenses associated with commercial 4D-CT hardware and software. We should continue to be aware of the limitations of contouring on MIPs, such as overwrite of the target volume by higher density surrounding tissue (23, 37, 38). However, methods

such as the generation of a weighted MIP address the overwrite and loss of contrast that occurs in regions near the diaphragm (28). Breathing irregularities such as coughing or deep inhalation may cause the tumor motion envelope to be exaggerated with both  $MIP_{CINE}$  and  $MIP_{4D-CT}$  (39). It may be advisable to consider an alternative method of respiratory monitoring to ensure that irregular breathing does not occur during the scan period.

## 6.2 Future Work

There are many opportunities for future work within the field of 4D-CT and target volume delineation. One strength of the current study lies in our identification of causes of MIP volume differences on clinical data. The findings may shed light on future improvements to methods of 4D-CT sorting. Our data show that the AB sorting method had the lowest average contoured iGTV, which suggests that modifications of the AB method should be considered. For example, the current AB method associates the nearest-neighbor amplitude value closest to the time-aligned image; alternatively, one could associate an *average* amplitude to each cine CT image by considering the amplitude values within the temporal window of each image. To test the feasibility, we applied this method to the example presented in Figure 26, and found that the correct maximum extent image was selected (image (c) in the figure).

While this study did not focus specifically on the low-pitch helical acquisition method of 4D-CT, there are some thematic similarities that may offer insight for further improvement. Information related to the identification of a maximum extent image may allow for a more appropriate sinogram binning mechanism. Users of helical 4D-CT should be aware of the potential for under-estimation of  $MIP_{4D-CT}$  in their iGTV delineation.

The final recommendation based on this work is that the  $MIP_{CINE}$  should be used as one of the tools to delineate the target volume. Our study has shown that the  $iGTV_{CINE}$  for tumors moving at least 1 cm is larger in magnitude than any of the  $iGTV_{4D-CT}$  values. Further studies should be performed to assess whether the margin expansion process should be modified while incorporating

the  $MIP_{CINE}$  for iGTV identification – while our results indicate that the resultant iGTV will be larger with  $MIP_{CINE}$  than with  $MIP_{4D-CT}$ , we expect the uncertainty in motion will decrease, possibly necessitating smaller margins (7).

Patients that were selected for the current study had tumors that were easily differentiable; we avoided the selection of lung tumors for which the diaphragm obscured the tumor motion envelope. Newer methods have been developed to address the issue of overlap between the diaphragm and the tumor motion envelope. One such method generates a weighted MIP whereby the user identifies and selects an image closest to the EI phase in the region of overlap. Results have indicated that selective inclusion of certain images can restore contrast to the tumor border (28). The ability to recover tumor contrast increases the possible applications of MIP in the assessment of tumor motion. Further study should be performed on a larger pool of patients to identify any potential negative aspects of creating a weighted MIP. If it is clinically feasible, the creation of a simple user-interface for clinical implementation is desirable.

Other methods of external respiratory tracking have been explored, such as the usage of spirometry to measure tidal volume or bellows to measure abdominal expansion (14). Usage of an external surrogate requires the assumption that the internal motion correlates to the motion of the external marker. One study by Ionascu *et al* found that, for a collection of 10 patients, the correlation between internal anatomy and external surrogate was good with motion along the SI direction, but was worse in the AP direction (40). Our study offered an example for which the correlation between internal anatomy and external surrogate was incorrect (See Figure 26), due to a combination of sorting methodology, the image temporal resolution, and phase lag. More recent research has focused on the correlation between an internal anatomical marker (such as the diaphragm) and the target volume motion. New research into methods such as internal gating may offer new insight into the best metric for tracking tumor motion.



## 7. CONCLUSIONS

In most cases exhibiting tumor motion of at least 1 cm, a MIP generated from a 4D-CT sorting method does a clinically adequate job of capturing the full extent of tumor motion. However, we observed clinical situations for which the iGTV was under-represented in the  $MIP_{4D-CT}$  by more than 10% when compared to the iGTV from  $MIP_{CINE}$ . To avoid potential geometric miss, we recommend use of the  $MIP_{CINE}$ , generated from all cine CT images, for contouring the target volume. With regard to the 4D-CT volume measurements, the PC-PB method had the largest average iGTV, followed by the PB method, then the AB method. The AB method was the most susceptible to selection of identical images for two adjacent image bins.

## 8. BIBLIOGRAPHY

1. Videtic, G. M., A. K. Singh, and J. Y. Chang. 2009. A randomized phase II study comparing 2 stereotactic body radiation therapy (SBRT) schedules for medically inoperable patients with stage I peripheral non-small cell lung cancer. Radiation Therapy Oncology Group RTOG 0915 (NCCTG N0927).
2. Wink, N., C. Panknin, and T. D. Solberg. 2006. Phase versus amplitude sorting of 4D-CT data. *Journal of applied clinical medical physics / American College of Medical Physics* 7:77-85.
3. Abdelnour, A. F., S. A. Nehmeh, T. Pan, J. L. Humm, P. Vernon, H. Schoder, K. E. Rosenzweig, G. S. Mageras, E. Yorke, S. M. Larson, and Y. E. Erdi. 2007. Phase and amplitude binning for 4D-CT imaging. *Physics in medicine and biology* 52:3515-3529.
4. Mayo, J. R., N. L. Muller, and R. M. Henkelman. 1987. The double-fissure sign: a motion artifact on thin-section CT scans. *Radiology* 165:580-581.
5. Crawford, C. R., K. F. King, C. J. Ritchie, and J. D. Godwin. 1996. Respiratory compensation in projection imaging using a magnification and displacement model. *IEEE transactions on medical imaging* 15:327-332.
6. Balter, J. M., R. K. Ten Haken, T. S. Lawrence, K. L. Lam, and J. M. Robertson. 1996. Uncertainties in CT-based radiation therapy treatment planning associated with patient breathing. *International journal of radiation oncology, biology, physics* 36:167-174.
7. Keall, P. J., G. S. Mageras, J. M. Balter, R. S. Emery, K. M. Forster, S. B. Jiang, J. M. Kapatoes, D. A. Low, M. J. Murphy, B. R. Murray, C. R. Ramsey, M. B. Van Herk, S. S. Vedam, J. W. Wong, and E. Yorke. 2006. The management of respiratory motion in radiation oncology report of AAPM Task Group 76. *Medical physics* 33:3874-3900.
8. Keall, P. J., V. R. Kini, S. S. Vedam, and R. Mohan. 2002. Potential radiotherapy improvements with respiratory gating. *Australasian physical & engineering sciences in*

- medicine / supported by the Australasian College of Physical Scientists in Medicine and the Australasian Association of Physical Sciences in Medicine 25:1-6.
9. Giraud, P., Y. De Rycke, B. Dubray, S. Helfre, D. Voican, L. Guo, J. C. Rosenwald, K. Keraudy, M. Housset, E. Touboul, and J. M. Cosset. 2001. Conformal radiotherapy (CRT) planning for lung cancer: analysis of intrathoracic organ motion during extreme phases of breathing. *International journal of radiation oncology, biology, physics* 51:1081-1092.
  10. Alasti, H., Y. B. Cho, A. D. Vandermeer, A. Abbas, B. Norrlinger, S. Shubbar, and A. Bezjak. 2006. A novel four-dimensional radiotherapy method for lung cancer: imaging, treatment planning and delivery. *Physics in medicine and biology* 51:3251-3267.
  11. ICRU. 1993. Prescribing, Recording and Reporting Photon Beam Therapy. In ICRU Report No 50, Bethesda, MD.
  12. ICRU. 1999. Prescribing, Recording and Reporting Photon Beam Therapy (Supplement to ICRU Report 50). In ICRU Report No 62, Bethesda, MD.
  13. Stevens, C. W., R. F. Munden, K. M. Forster, J. F. Kelly, Z. Liao, G. Starkschall, S. Tucker, and R. Komaki. 2001. Respiratory-driven lung tumor motion is independent of tumor size, tumor location, and pulmonary function. *International journal of radiation oncology, biology, physics* 51:62-68.
  14. Lu, W., P. J. Parikh, J. P. Hubenschmidt, J. D. Bradley, and D. A. Low. 2006. A comparison between amplitude sorting and phase-angle sorting using external respiratory measurement for 4D CT. *Medical physics* 33:2964-2974.
  15. Pan, T., T. Y. Lee, E. Rietzel, and G. T. Chen. 2004. 4D-CT imaging of a volume influenced by respiratory motion on multi-slice CT. *Medical physics* 31:333-340.
  16. Keall, P. J., G. Starkschall, H. Shukla, K. M. Forster, V. Ortiz, C. W. Stevens, S. S. Vedam, R. George, T. Guerrero, and R. Mohan. 2004. Acquiring 4D thoracic CT scans using a multislice helical method. *Physics in medicine and biology* 49:2053-2067.

17. Pan, T. 2005. Comparison of helical and cine acquisitions for 4D-CT imaging with multislice CT. *Medical physics* 32:627-634.
18. Ford, E. C., G. S. Mageras, E. Yorke, and C. C. Ling. 2003. Respiration-correlated spiral CT: a method of measuring respiratory-induced anatomic motion for radiation treatment planning. *Medical physics* 30:88-97.
19. Vedam, S. S., P. J. Keall, V. R. Kini, H. Mostafavi, H. P. Shukla, and R. Mohan. 2003. Acquiring a four-dimensional computed tomography dataset using an external respiratory signal. *Physics in medicine and biology* 48:45-62.
20. Pan, T., X. Sun, and D. Luo. 2007. Improvement of the cine-CT based 4D-CT imaging. *Medical physics* 34:4499-4503.
21. Rietzel, E., A. K. Liu, G. T. Chen, and N. C. Choi. 2008. Maximum-intensity volumes for fast contouring of lung tumors including respiratory motion in 4DCT planning. *International journal of radiation oncology, biology, physics* 71:1245-1252.
22. Park, K., L. Huang, H. Gagne, and L. Papiez. 2009. Do maximum intensity projection images truly capture tumor motion? *International journal of radiation oncology, biology, physics* 73:618-625.
23. Rietzel, E., G. T. Chen, N. C. Choi, and C. G. Willet. 2005. Four-dimensional image-based treatment planning: Target volume segmentation and dose calculation in the presence of respiratory motion. *International journal of radiation oncology, biology, physics* 61:1535-1550.
24. Henkelman, R. M., and K. Mah. 1982. How important is breathing in radiation therapy of the thorax? *International journal of radiation oncology, biology, physics* 8:2005-2010.
25. Bushberg, J. T., J. A. Seibert, E. M. Leidholdt, and J. M. Boone. 2002. *The essential physics of medical imaging*. Lippincott Williams and Wilkins, Philadelphia, PA.
26. Podgorsak, E. B. 2005. *Radiation Oncology Physics: A Handbook for Teachers and Students*. IAEA, Vienna, Austria.

27. Steel, G. G., editor. 2002. Basic Clinical Radiobiology. Hodder Arnold, New York.
28. Pan, T., J. Chang, A. Riegel, M. Ahmad, X. Sun, and D. Luo. 2008. SU-GG-J-138: New Weighted Maximum Intensity Projection (MIP) Images for Assessing Tumor Motion in the Thorax Without a Respiratory Surrogate. AAPM. 2710-2711.
29. Rietzel, E., T. Pan, and G. T. Chen. 2005. Four-dimensional computed tomography: image formation and clinical protocol. Medical physics 32:874-889.
30. Chi, P. C., P. Balter, D. Luo, R. Mohan, and T. Pan. 2006. Relation of external surface to internal tumor motion studied with cine CT. Medical physics 33:3116-3123.
31. Chang, G., T. Chang, J. W. Clark, Jr., and O. R. Mawlawi. Design and performance of a respiratory amplitude gating device for PET/CT imaging. Medical physics 37:1408-1412.
32. Pan, T., O. Mawlawi, D. Luo, H. H. Liu, P. C. Chi, M. V. Mar, G. Gladish, M. Truong, J. Erasmus, Jr., Z. Liao, and H. A. Macapinlac. 2006. Attenuation correction of PET cardiac data with low-dose average CT in PET/CT. Medical physics 33:3931-3938.
33. Philips. 2005. Pinnacle Planning: Instructions for Use. In Document Number 9201-5121A-ENG A.
34. Mutaf, Y. D., J. A. Antolak, and D. H. Brinkmann. 2007. The impact of temporal inaccuracies on 4DCT image quality. Medical physics 34:1615-1622.
35. Riegel, A. C., J. Y. Chang, S. S. Vedam, V. Johnson, P. C. Chi, and T. Pan. 2009. Cine computed tomography without respiratory surrogate in planning stereotactic radiotherapy for non-small-cell lung cancer. International journal of radiation oncology, biology, physics 73:433-441.
36. Hui, H., T. Pan, and Y. Shen. 2000. Multislice helical CT: image temporal resolution. IEEE transactions on medical imaging 19:384-390.
37. Underberg, R. W., F. J. Lagerwaard, B. J. Slotman, J. P. Cuijpers, and S. Senan. 2005. Use of maximum intensity projections (MIP) for target volume generation in 4DCT scans for lung cancer. International journal of radiation oncology, biology, physics 63:253-260.

38. Bradley, J. D., A. N. Nofal, I. M. El Naqa, W. Lu, J. Liu, J. Hubenschmidt, D. A. Low, R. E. Drzymala, and D. Khullar. 2006. Comparison of helical, maximum intensity projection (MIP), and averaged intensity (AI) 4D CT imaging for stereotactic body radiation therapy (SBRT) planning in lung cancer. *Radiother Oncol* 81:264-268.
39. Starkschall, G., N. Desai, P. Balter, K. Prado, D. Luo, D. Cody, and T. Pan. 2007. Quantitative assessment of four-dimensional computed tomography image acquisition quality. *Journal of applied clinical medical physics / American College of Medical Physics* 8:2362.
40. Ionascu, D., S. B. Jiang, S. Nishioka, H. Shirato, and R. I. Berbeco. 2007. Internal-external correlation investigations of respiratory induced motion of lung tumors. *Medical physics* 34:3893-3903.

## **9. VITA**

David Anthony Zamora was born in Ft. Stockton, Texas on April 5, 1982, the son of Jesús Ernesto Zamora and Jeaneen Ann Zamora. He lived in Midland, TX and Portland, TX before graduating from Gregory-Portland High School. He began his undergraduate work at the University of Texas at Austin in 2000, and received a B.S. in mechanical engineering in August 2004. After graduation he accepted a position as a physics technologist at The University of Texas MD Anderson Cancer Center, Department of Imaging Physics. In August 2008, he entered The University of Texas Health Science Center at Houston Graduate School of Biomedical Sciences.

Permanent Address:  
11207 Oak View Dr.  
Austin, TX 78759